



Reliability-aware collapse-resisting design of precast concrete beam–column joints using strengthened steel angles and high-strength bolts

Zidong Zhao^a, Marcos A. Valdebenito^b, Yi Li^{a,*}, Chao Dang^{b,*}, Weijing Zhang^a, Matthias G.R. Faes^{b,c}

^a Beijing Key Laboratory of Earthquake Engineering and Structural Retrofit, Beijing University of Technology, Beijing 100124, China

^b Chair for Reliability Engineering, TU Dortmund University, Leonhard-Euler-Straße 5, Dortmund 44227, Germany

^c International Joint Research Center for Engineering Reliability and Stochastic Mechanics, Tongji University, Shanghai 200092, China

ARTICLE INFO

Keywords:

Dry beam–column connection
Simplified model
Active learning probabilistic integration
Small failure probability assessment
Global sensitivity analysis
Reliability sensitivity analysis

ABSTRACT

Beam–column joint connections are critical for precast concrete frames to resist collapse, yet their internal load transfer mechanisms and demand-side uncertainties remain underexplored. This study develops a preliminary reliability-aware collapse-resisting design framework for a high-performance dry connection, incorporating strengthened steel angles and high-strength bolts. The design part begins with the identification of load transfer mechanisms and configuration optimization to eliminate undesirable failure modes based on detailed finite element models. Thereby the design focuses on estimating the upper-bound of the column bolt axial force demand, derived based on rebar ultimate strengths. The reliability assessment of the derived demand relies on: (1) a newly developed and validated macro joint model, alleviating the computational burden of repeated model evaluations; and (2) a modified active learning probabilistic integration method ensuring highly efficient reliability assessment using a small number of model evaluations. The learning function and the point selection strategy are tailored to the highly nonlinear nature of the involved performance function. Material uncertainties in the structural components connected by the joint are explicitly considered because they significantly influence joint demands. Moreover, variance-based global sensitivity analysis and local reliability sensitivity analysis are performed by post-processing the Gaussian process regression model obtained from the reliability assessment. The results indicate that the rebar ultimate strength, yield strength, and fracture strain are the most influential random variables affecting the design reliability. Their mean values are recommended to be explicitly considered in the design phase in future research; tighter quality control on rebar production, aimed at reducing material property variability, can further improve the design reliability.

1. Introduction

Structural progressive collapse is a system-level failure phenomenon that initiates from a local failure, caused by accidental loads or construction defects, which triggers a chain reaction of damage propagation throughout the connected structural system. This cascading failure ultimately leads to a collapse disproportionate to the initial cause, generally leading to catastrophic consequences [1–3]. To mitigate the structural collapse, several design codes and regulations [4–8] have introduced collapse-resisting design strategies. Extensive studies have been conducted on reinforced concrete (RC) frame structures, showing that they engage sequential resistance mechanisms: beam flexural action, compressive arch action (CAA) [9–11], and catenary action (CA)

[12–14], during progressive collapse. The maximum vertical deformation can exceed one-fifth of the clear beam span [6], imposing substantial demands on the performance and integrity of the beam–column joints, which become the critical part in mitigating progressive collapse.

Despite the merits provided by the deterministic analysis, the inherent uncertainties involved in the structures are also imperative to be considered [15,16], and due to the data scarcity on accidental loads and corresponding initial local failure, the probabilistic analysis mainly focused on the structural collapse resisting behavior itself. Brunesi et al. [17] derived a fragility function-based structural robustness assessment method, indicating that the robustness could be increased when seismic detailing and second beams were involved. Li et al. [18] proposed a collapse probability index for structural collapse considering all initial

* Corresponding authors.

E-mail addresses: yili@bjut.edu.cn (Y. Li), chao.dang@tu-dortmund.de (C. Dang).

<https://doi.org/10.1016/j.strusafe.2026.102710>

Received 21 July 2025; Received in revised form 10 February 2026; Accepted 13 March 2026

Available online 23 March 2026

0167-4730/© 2026 The Author(s). Published by Elsevier Ltd. This is an open access article under the CC BY license (<http://creativecommons.org/licenses/by/4.0/>).

local failures of critical load-bearing components, and derived a simplified fragility curve under different gravity load levels. More specifically, Yu et al. [19] focused on uncertainties of the frame structure in resisting progressive collapse under certain column removal scenarios, identifying that the gravity load and reinforcement properties were two critical types of uncertainties affecting collapse resisting performance. Feng et al. [20] and Gan et al. [15] proposed different robustness quantification frameworks without and with considering the initial failure, respectively; Lin et al. [21] employed an energy-based method to quantify the structural collapse resisting-capacity under dynamic scenarios. Similarly, Ding et al. [22] provided the quantification of model uncertainties of the energy-based method in dynamic column removal scenarios, and then Ding and Chen [23] established a collapse failure criteria. Furthermore, Ribeiro et al. [24] also managed to derive a risk-based collapse-resisting design framework for RC frame structures considering different level of local failure probabilities.

Notably, prior studies have primarily focused on reliability analysis at the global level of RC frame structures, without requiring a dedicated investigation of joint connectivity, as the joints are cast monolithically with adjacent members. However, in precast concrete (PC) frame structures, especially for those employing dry connections which offer advantages in construction speed and quality control [25], the effectiveness of joint connectivity must first be ensured. Given the inherent uncertainties in RC structural components, particularly those associated with material properties, the demand imposed on the joint connectivity during collapse scenarios is also influenced. As a result, ensuring the joint's capacity under such uncertain demand conditions is essential for the overall collapse resistance of PC frames, which are composed of different types of RC structural components connected by joints. This aspect has not received as much attention in existing studies [16], where the major focus has been on deterministic assessments of collapse resistance for various types of dry connections [26–28] and their resisting mechanisms at the structural level [27,29,30]. This disconnection highlights at least two gaps existing in the literature, namely: the lack of a targeted joint demand design that captures the joint distinct load transferring mechanisms under collapse conditions; and the absence of uncertainty quantification for the joint demand induced by the material variability of connected structural components. This study aims to address both gaps to develop a high-reliability dry connection with robust collapse resisting performance.

To address the first gap, namely the lack of a collapse-resisting design for joint connections, a series of deterministic analyses are conducted in this study. A high performance beam–column connection, utilizing steel angles and high-strength bolts [27,29,31], is firstly selected as the study object, due to its superior joint integrity compared to corbel-bolt connections [25,28,32,33] and direct welding connections [26,34,35]. A finite element (FE) model-based connection optimization is then performed to avoid undesired joint failure modes, followed by identification of its distinct load transfer mechanism. On such a basis, an upper bound of the joint demand is derived and adopted as a design target for the reliability-aware connection design.

The second gap lies in efficient reliability analysis of the derived demand, which might involve costly model evaluations and quite small failure probabilities, making some traditional reliability analysis approaches [17,21] infeasible due to a substantial number of model evaluations required. Therefore, in this study, a macro joint model is developed and validated as a simplification for the costly detailed FE model, while preserving sufficient fidelity for reliability estimations; the active learning probabilistic integration (ALPI) method [36,37] that can efficiently assess small failure probabilities is adopted, and the learning function is modified to select the most informative and diverse evaluation points.

This work is organized as follows. The first step consists of selecting the type of connection along with the development and validation of a FE model. This is discussed in Sections 2 and 3. On this basis, key contributions of this study are: 1) configuration optimization and

identification of connection load transfer mechanisms, and the derivation of the collapse-resisting design method (Section 4); 2) establishment of a macro joint model that captures the joint load transfer mechanisms whose numerical evaluation is inexpensive while preserving sufficient prediction fidelity (Section 5); 3) modification of the ALPI method for reliability assessment of strongly nonlinear structural collapse problems, (Section 6); 4) global sensitivity analysis and reliability sensitivity analysis by post-processing the Gaussian process (GP) regression model obtained from the reliability assessment, identifying both the most influential random variables and their corresponding most influential distribution parameters (Section 7). Finally, concluding remarks are given in Section 8.

2. Overview of the studied joint connection

The joint connection selected consists of strengthened steel angles and high-strength bolts, as shown in Fig. 1. The bolts installed on the column and beam are connected via the strengthened steel angles, enabling load transfer as the beam deforms during collapse. This joint design was proposed in previous studies [29,31] as an improvement over earlier versions employing ordinary steel angles; it primarily underwent flexural deformation and tended either to fail in the early stages of collapse or to induce excessive torsional stress in the column bolts, eventually leading to bolt fracture that contradicted conservative design expectations [31]. Such failure modes are difficult to control and should therefore be avoided. Accordingly, it becomes evident that by incorporating ribs onto steel angles, namely the strengthened steel angle, the load transfer between the beam and column bolts can be effectively maintained, and undesired irregular bolt deformations can be alleviated in the meantime. In addition, the load transfer between the beam internal force and the joint should also be ensured. Therefore, a welding anchorage for the longitudinal rebars in the beam ends is introduced. As displayed in Fig. 1, the rebar ends are welded to embedded steel plates at the beam ends, which then transfer the rebar axial force to the beam bolts. As a result, the primary load transfer path in the joint region follows the path: beam longitudinal rebars (concrete)—embedded steel plates—beam bolts—steel angles—column bolts—column.

Although previous studies have examined the performance of the joint connection under collapse scenarios [29,31], its underlying load transfer mechanism remains unclear due to limitations in data acquisition in a collapse test. Therefore, the finite element (FE) model is employed herein to enable a detailed analysis of the internal force development within the joint region. Accordingly, the loading condition effects and further configuration optimization for the joint are investigated first, and the corresponding joint design method is developed in following sections.

3. Detailed FE model establishment and validation

3.1. Experimental basis from prior work

In the present study, the FE model is established using LS-DYNA, and

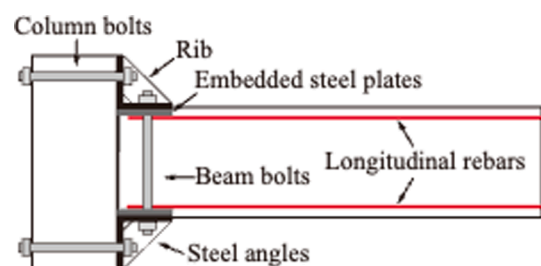


Fig. 1. Joint connection utilizing strengthened steel angles and high-strength bolts.

validated based on progressive collapse analysis on the PC beam-column assembly employing the corresponding dry connection scheme. The assembly includes two beam-spans, one middle column stub, and two side columns with the right-hand one being connected to a beam extension, as elaborated in Fig. 2. In addition, the cubic concrete strength is 43.5 MPa, and the grouting cement mortar bending strength is 88 MPa. All the other material properties are available in [29]. The test setup is displayed in Fig. 3. The assembly was constrained by pin-pin connections to the reaction frame at top of both the side columns and the beam extension, and pinned supports at bottom of the side columns, which were exerted an axial force of 200 kN through a self-balance loading system. After exerting the axial load, a uniformly distributed load was applied, as shown in Fig. 3.

3.2. FE model establishment

This section presents the general modelling strategy, while detailed information is provided in Appendix A, including distinct modelling settings for the joint and restraints adopted from previous FE studies [31,38]. The simulations are conducted on a workstation equipped with an Intel Core i9-12900 K CPU and 128 GB RAM. The FE model contains 132,506 elements, and the total number of degrees of freedom is approximately 526,863. The wall-clock computation time for one analysis is approximately 20 h.

3.2.1. Element types and material models

The numerical model is shown in Fig. 4. Concrete and steel components are modelled using 8-node solid elements with single-integration point, while the rebars and bolts are modelled using 2-node Hughes-Liu beam elements with 2×2 Gauss quadrature integration [39]. Rebars embedded in concrete are modelled using an embedded-beam-in-solid coupling approach. The continuous surface cap model is adopted for concrete [30,39,40] and a piecewise linear plastic model is adopted for rebars and steel components [31]. The dry connection joint is fully replicated in the FE model, and the details are explained in Appendix A.

3.2.2. Boundary conditions and loading methods

In the FE model, the horizontal restraint, the pinned supports, the self-balanced axial loading system, and the load distribution device are modelled using methods reported in [31,38]. The axial stiffness of the horizontal restraint is determined to be 15000 N/mm here. At all free ends of the connections and at supports away from the assembly, the nodes are fully restrained in all degrees of freedom. In addition, out-of-plane constraints are implemented by constraining the translational degree of freedom in y-axis of the beam. A displacement load is applied on top of the load distribution device, as seen in Fig. 4.

3.3. Comparisons between the simulation and the experimental results

Fig. 5 shows comparisons of load and horizontal reaction force of the FE model against the test results. During the experiment, when the middle joint displacement (MJD) exceeded 300 mm, the loading point

on the device became jammed, making the subsequent response strongly test-setup-specific, instead of depending purely on the structural response [29]. As shown in Fig. 5, when the MJD approaching 300 mm, a slight re-increase of the load is observed followed by a sharp increase due to a fully jammed condition of the loading points. Therefore, validation of the FE model's accuracy is confined to structural responses prior to a MJD of 300 mm. The FE model shows a bit higher initial loading stiffness compared to the test specimen, mainly due to the simulation of the complex set-up of the horizontal restraints. In the test, each horizontal restraint consists of bolts, load cells, and joint revolutes, and their connection/interaction behaviors may change during the loading process, for instance, due to clearance, friction, or slight slippage. These behaviors are hard to quantify and be implemented in the FE model. Therefore, the primary objective of the numerical model is to achieve overall agreement with the experiment.

The corresponding deviations regarding the first peak load and the maximum compressive horizontal reaction force are 4% and 11%, respectively. The damage patterns at this deformation state are also compared in Fig. 6. In the FE model, the damage condition is represented by the distribution of the effective plastic strain which can be interpreted as concrete crack developments, and element deletion that refers to severe concrete damage [39]. The comparison results demonstrate that the FE model accurately reproduces the observed damage patterns.

Notably, the validation range covers the relatively complex progressive collapse stage governed by CAA, in which the beam and joint region are subjected to combined bending and axial compression. After this stage, the specimen would transition toward the CA stage, where the joint response is dominated by axial tension transferred from the beam longitudinal rebars [30]. This loading state is comparatively simpler and can be captured by the established model, as evidenced in our prior study on similar joint and structural configurations [31].

In summary, the FE model has undergone rigorous validation, exhibiting high simulation accuracy. The model suitability is then established for subsequent joint load transfer analyses and the calibration of simplified models.

4. Axial force demand estimation method of high-strength bolts from a collapse-resisting perspective

Building upon the validated FE model, this section conducts an internal force analysis to identify the loading condition that generates the highest demand on the joint. In parallel, the deformation behavior of the steel angle during collapse is closely examined, as the ribbed steel angle may exhibit irregular deformation under ultimate collapse conditions due to its complex geometry. This deformation is difficult to quantify through theoretical calculations and can induce undesired stress concentrations in the column bolts, potentially leading to unexpected failure, as discussed in Section 2. To address this issue, a configuration optimization of the steel angle is performed using the FE model, which helps mitigate such irregularities and facilitates the subsequent design process. With the steel angle deformation effectively controlled, the

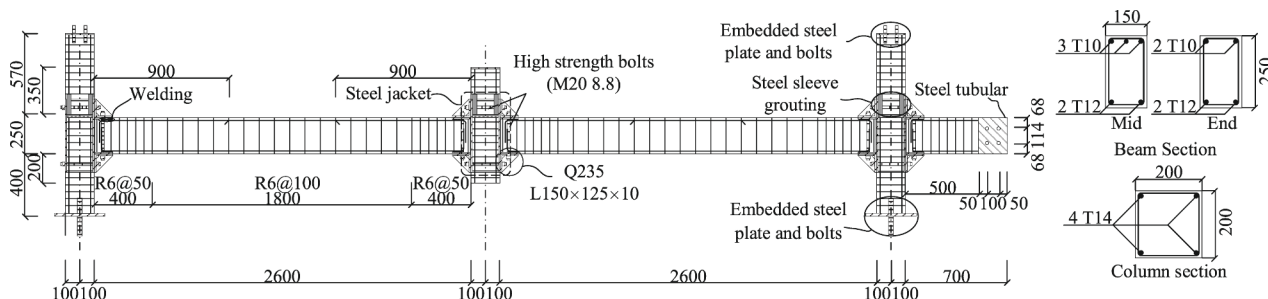


Fig. 2. PC beam-column assembly configurations (Unit: mm).

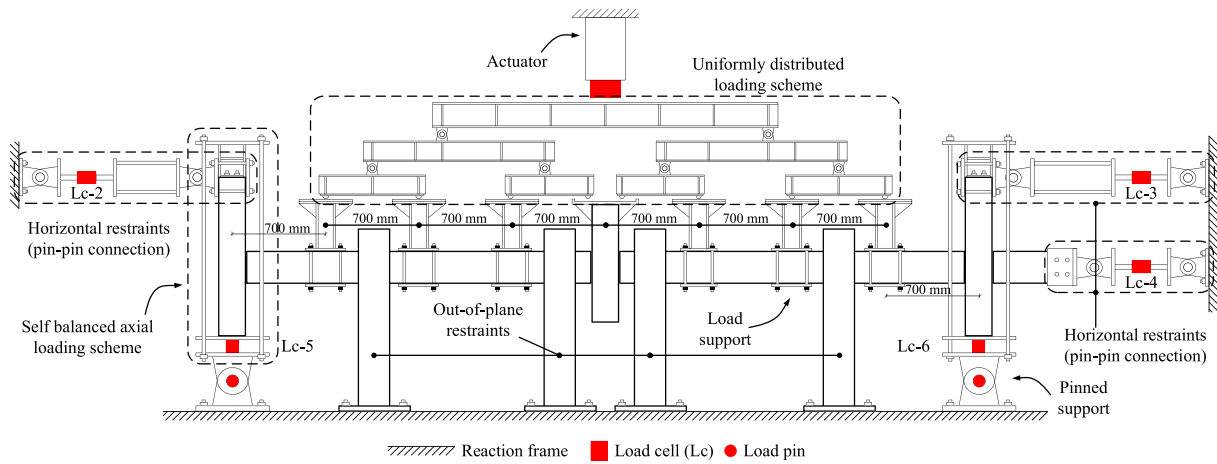


Fig. 3. Progressive collapse test setup: loading method and boundary conditions.

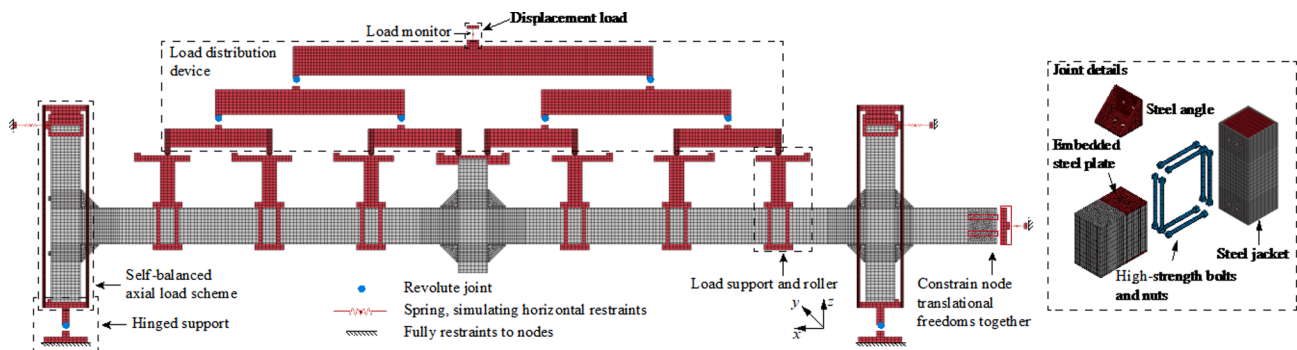


Fig. 4. Geometric model of the beam-column assembly and joint details.

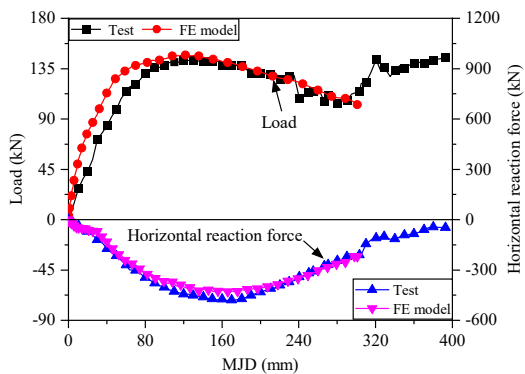


Fig. 5. Load and horizontal reaction force.

design focus shifts to estimating the axial force demand in the column bolts, based on an understanding of the load transfer mechanism within the joint region.

4.1. Loading condition effects

Pham and Tan [41], and Qian et al. [42] showed that different loading conditions, i.e., concentrated load (CL) on the lost column and uniformly distributed load (UDL) on the beam components, can induce distinct collapse responses in beam-column assemblies. Therefore, the loading condition effects on the joint internal force development is investigated with the middle joint being loaded up to 600 mm, exceeding 1/5 of the clear beam span (i.e., 520 mm) to satisfy the DoD regulation [6]. Fig. 7 shows that the bolt axial force experiences an

initial peak during the CAA stage, but the largest bolt axial force is induced in the CA stage, at the end of the collapse process. The overall trend is comparable under UDL and CL, with a marginal difference between the maximum bolt forces under UDL (108 kN) and CL (100 kN) for the side and middle column sections, respectively.

The relationships between the beam end rebar tensile strain and the MJD, as well as between the bolt axial force and the rebar tensile strain, are further explored, as shown in Figs. 8 and 9. It is evident that for achieving the same level of the MJD in large deformation range, the tensile strain demand on the rebar is significantly higher under UDL, compared to CL. The peak tensile strain under UDL even exceeds 0.6, as UDL induces a significantly large beam end rotation [29], which is nearly unachievable in practice. Furthermore, Fig. 9 demonstrates that the bolt axial force under CL exceeds that under UDL as rebar tensile strain exceeds 0.08—approximately corresponding to the point at which the rebar in the compressive region transitions into tension, since the transition occurs earlier under CL (i.e., at a strain of 0.09) than under UDL (i.e., 0.24), as shown in Fig. 10. After both the top and bottom rebars at the beam end enter tension, the bolts are subjected to greater bending moments transferred from the rebars—more so under CL than under UDL.

In summary, although UDL yields a slightly higher peak bolt axial force, it requires unrealistic rebar strain to reach such deformation. In contrast, the CL condition produces greater bolt axial force in a more feasible strain range and induces more significant force transfer due to earlier transition to tension state of both rebar layers. Therefore, the CL condition should be regarded as a critical loading condition for following development of the design method.

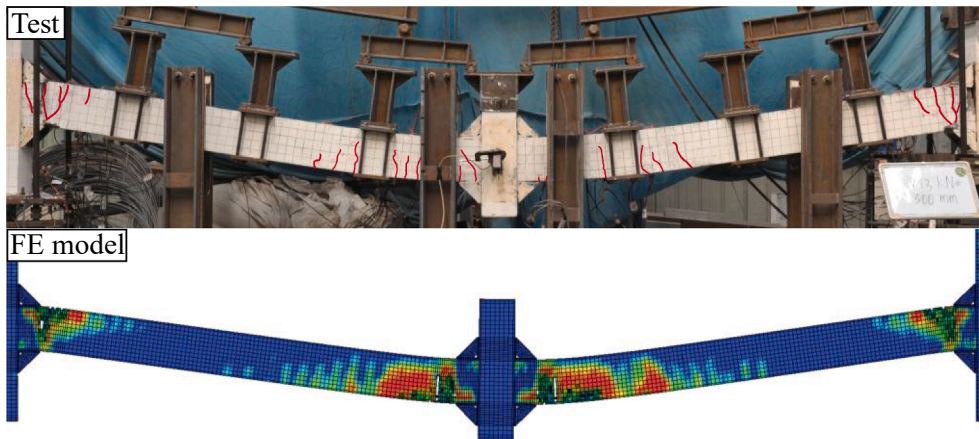


Fig. 6. Damage patterns when MJD reaching 300 mm.

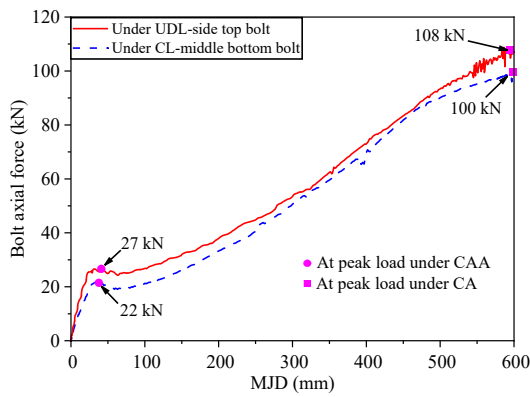


Fig. 7. Bolt axial force–MJD.

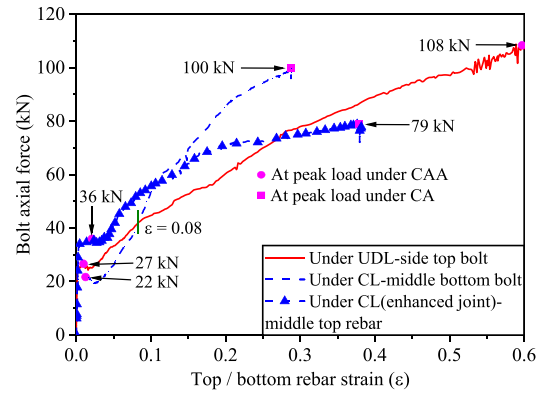


Fig. 9. Bolt axial force–rebar tensile strain.

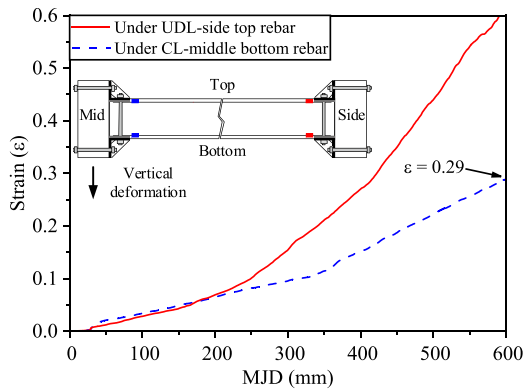


Fig. 8. Rebar tensile strain–MJD.

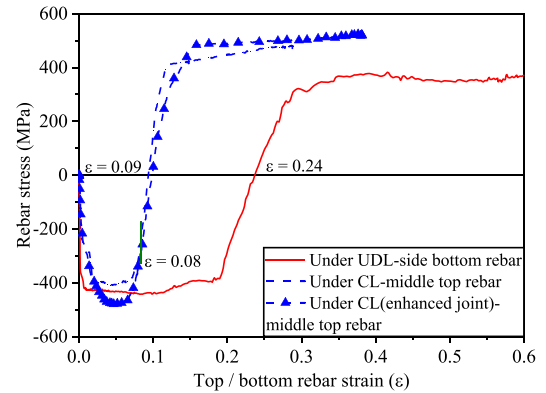


Fig. 10. Stress of compressive region rebar.

4.2. Optimization of the steel angle configuration

As outlined in Section 2 and reiterated at the beginning of this section, irregular deformation of the steel angle should be avoided, as it is difficult to control and quantify, especially with regard to its adverse effects on the bolts. To this end, a FE model-based optimization of the steel angle configuration is performed.

Through trial and error, the optimized configuration is demonstrated in Fig. 11. A central rib is added at the midpoint between the bolt holes, to suppress local buckling. Besides, the number of bolts on the beam side is doubled relative to that on the column side to ensure a tight connection between the steel angle and the beam, thereby avoiding

undesired localized deformation that could complicate the design procedure. The final deformation states of the steel angle before and after optimization are displayed in Fig. 12. Using the optimized configuration, the steel angle only enters a minor yield state and experiences tiny deformation when the beam–column assembly enters the final collapse state. The corresponding maximum von Mises stress is 269 MPa, approximate to the yield stress 262 MPa. However, the original steel angle deforms obviously and irregularly, with the maximum stress reaching 371 MPa.

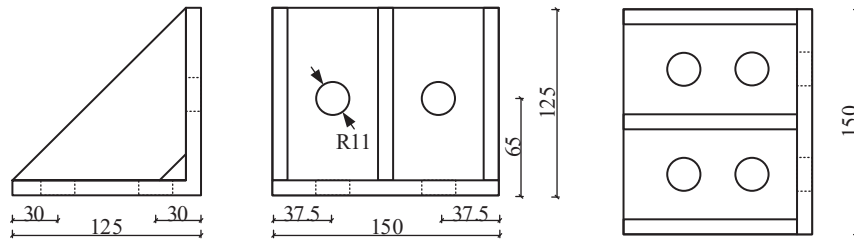


Fig. 11. Optimized configuration of steel angle.

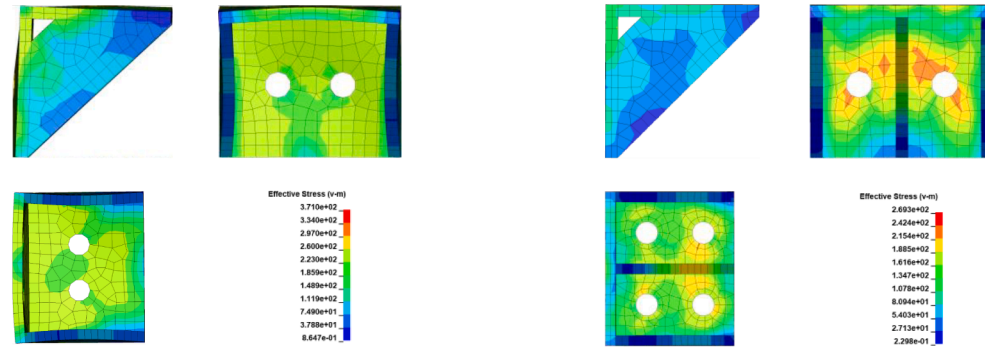
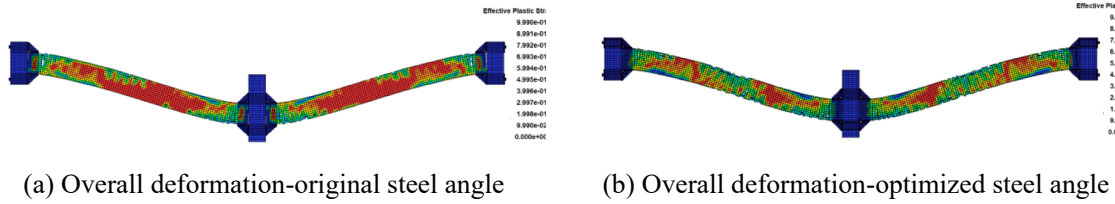


Fig. 12. Steel angle deformation state.

4.3. Development of estimation method of upper bound of the bolt axial force

Before deriving a bolt force estimation method—key for the collapse-resisting design of the joint—the load transfer mechanism is first explored to provide theoretical support. The fact that both top and bottom rebars are in tension suggests that the entire cross-section is subjected to a tensile state at the ultimate state in the CA stage. Therefore, the load diagram of the joint at the ultimate state can be interpreted as that shown in Fig. 13: 1) the collapse resistance P is provided by the vertical component of the rebar axial force; 2) by considering a tiny rotation of the whole beam end, including the steel angles, about the top edge of the upper steel angle, the bolt axial force and the rebars are expected to contribute comparable moments with respect to the rotation center.

Corresponding force equilibriums to be checked are listed as follows:

$$P' = 2(F_{RT} + F_{RB})\sin\theta, \tag{1}$$

$$M_B = F_{BT}(l_s - l_b) + F_{BB}(l_s + l_b + h), \tag{2}$$

$$M_R = F_{RT}\cos\theta(l_{ct} + l_s) + F_{RB}\cos\theta(h - l_{cb} + l_s) + (F_{RT} + F_{RB})\sin\theta l_s, \tag{3}$$

where, P' is the calculated collapse resistance based on the rebar axial force, and F_{RB} and F_{RT} are the total axial forces of the bottom and top rebars, respectively; M_B and M_R are the moments contributed from the column bolts and rebars, respectively, while F_{BT} and F_{BB} are the total axial forces of the top and bottom bolts, respectively; l_s and l_b are the lengths of the steel angle and distance from the bolt to the beam surface, respectively; l_{ct} and l_{cb} are the top and bottom rebar distances from rebar center to the top and bottom surface, respectively, and θ is the rotation of the beam that can be calculated by

$$\theta = \arctan \frac{\Delta}{L}, \tag{4}$$

where, Δ refers to the MJD in this study that is determined as 600 mm, and L is the clear span between the joint edges, namely 2350 mm.

The calculated collapse resistance P' is 127 kN, only 1% smaller than the FE model result of 128 kN; the moment contribution from the column bolts and rebars are 72 kN·m and 71 kN·m, respectively, of which the discrepancy is also only 1%. These good agreements show the adequateness of the load diagram. Based on this, the upper bound of the column bolt axial force, F_{UB} can be derived following two principles: 1)

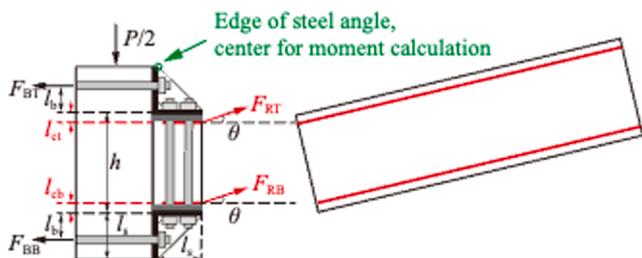


Fig. 13. Load diagram of joint under final collapse state.

in the ultimate state, the rebar in the initial compression region approaches the ultimate strength in tension (518 MPa to 595 MPa), the corresponding estimation then adopts a stress state of both top and bottom rebars reaching ultimate strengths; 2) the top column bolt contribution is omitted. Finally, the estimation can be done using:

$$F_{UB} = \frac{F_{RT} \cos\theta(l_{ct} + l_s) + F_{RB} \cos\theta(h - l_{cb} + l_s) + (F_{RT} + F_{RB}) \sin\theta l_s}{h + l_s + l_b}, \quad (5)$$

where for this case, the estimated value is 85 kN, 8% greater than the actual axial force. Notably, this function does not take into account the effect of fractures of the rebar, as the ultimate strength is assumed for both layers of the rebars to be conservative. Nevertheless, rebar fracture should be involved in estimation of the real bolt force, as it affects the final rebar stress state.

5. Development and validation of the simplified model considering the joint details

5.1. Model configuration and macro joint

The simplified model is displayed in Fig. 14, which is established on the basis of the detailed model with optimized steel angles, and shares similar boundary conditions. The software LS-DYNA is also utilized due to its proven excellent collapse simulation capacity using even the fiber model [15,43] and the purpose of using the same solving algorithm for the detailed and simplified model. The beam section is partitioned into several fibers with different integrations for concrete and rebars. The macro joint model is composed of boundary elements, a series of spring elements, and co-displacement constraints, as shown in Fig. 14. For the bolt springs, a nonlinear elastic spring model is adopted to define their mechanical behaviors, which are marked in a red color. They share the same characteristics with the column spring in compression, to capture the nearly incompressible column with steel tubular section. However, considering that the beam and column components are merely connected by the bolts, the tensile mechanical property, which is determined by the bolt dimensions and its mechanical property directly, is only involved in the bolt springs, as illustrated at the bottom of Fig. 14. The bolt springs are located according to the real joint configuration, while the co-displacement constraints are set at the bottom and top of the steel angle edge at the side and middle column, respectively, consistent with the load diagram discussed above.

5.2. Element type and material model

The Hughes-Liu beam element is adopted for the boundary, beam end, and fiber beams. The piecewise linear plastic model is adopted for the boundary elements with the elastic modulus being set as 2×10^4 GPa to ensure its stiffness. The joint beam ends are set as rigid, connected to the boundary elements. Each integration point in the fiber beam elements adopts the same material model that can simulate both the concrete and rebar behavior. For the concrete, the confinement effect is implemented by increasing the uniaxial compressive strength based on the Mander's model [44]. For the rebars, a typical stress-strain relationship is adopted, comprising an elastic stage, a yield plateau, and a strain-hardening stage. And the rebar fracture is activated when its axial stress exceeds a predefined value. Details of the simplified model establishment are illustrated in Appendix A.

5.3. Simplified model validation

As discussed in Section 4, both the ultimate strength and fracture strain of the rebars are critical for accurately estimating the maximum bolt axial force. To validate the effectiveness of the proposed simplified FE model, three pairs of detailed and simplified models are established using varying rebar ultimate strengths and fracture strain values. The selected ultimate strengths include 595 MPa in models D1 and S1 (from the selected experimental test), 547 MPa in models D2 and S2 (an additional sampled value), and 517 MPa in models D3 and S3 (the statistical mean value, to be presented in a subsequent section). Corresponding fracture strains are 0.137 (experimental value), 0.13 (sampled value), and 0.12 (statistical mean). Note that D and S refer to the detailed and simplified FE models for simplicity.

Fig. 15 displays the comparison of the load-displacement curves and bolt axial force development with increasing MJDs between the detailed and simplified FE models. In general, the load-displacement curve agrees well between the two types of FE models, and the rebar fracture in the simplified model is also simulated well compared to the detailed one. As the simplified model accounts only for the axial mechanical behavior of the bolt, the resulting axial force is underestimated compared to the detailed model in the CAA stage. However, with the assembly entering the CA stage, the bolt force replication becomes accurate with the maximum deviation being 4%, since the joint model is developed based on the load transfer characteristics in this stage.

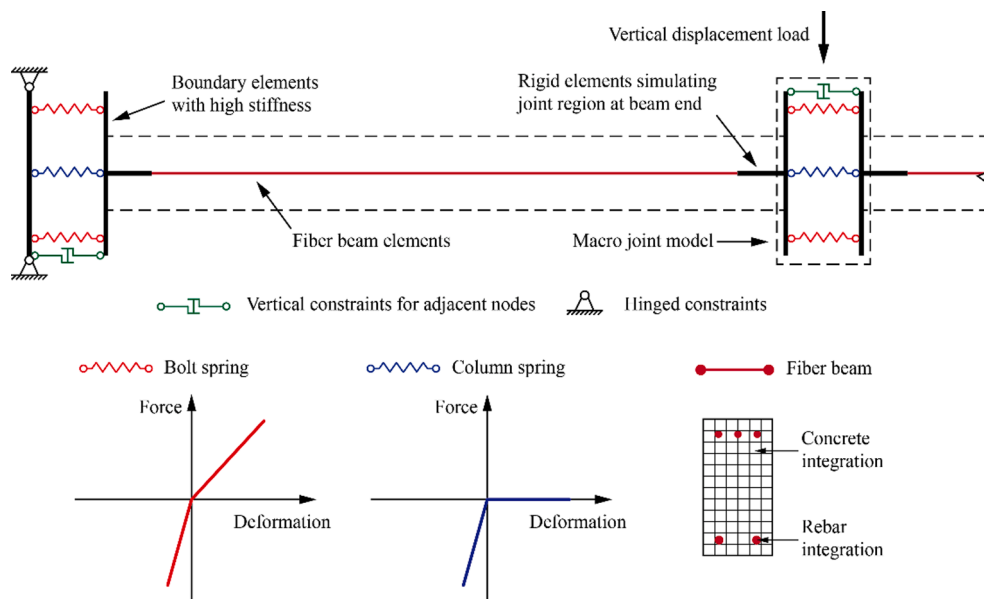


Fig. 14. Simplified model.

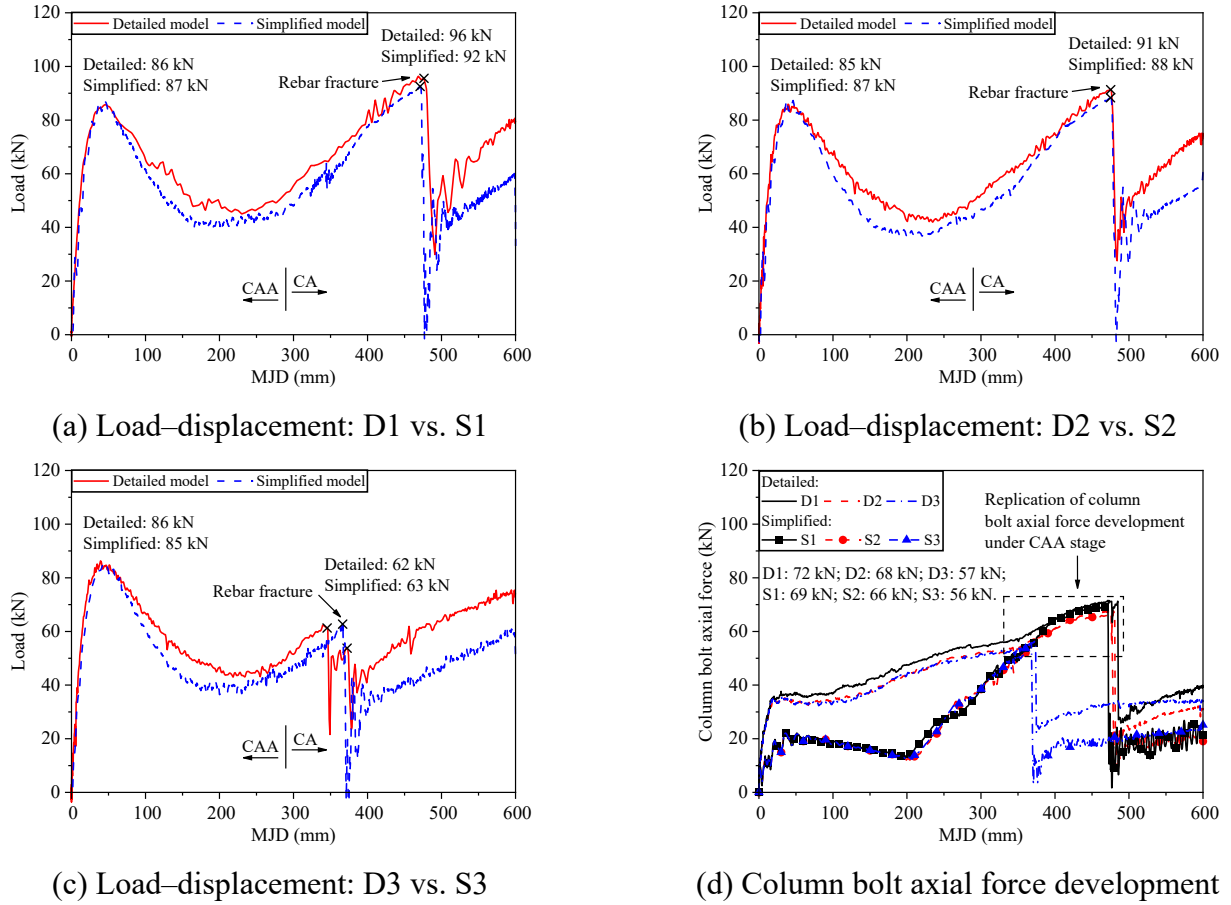


Fig. 15. Result comparisons between detailed and simplified model.

Furthermore, given that the primary objective of the simplified model is to capture the maximum (ultimate) column bolt axial force, the underestimation observed in the CAA stage does not compromise the failure prediction. Therefore, the simplified model is considered suitable for use in subsequent reliability analysis.

6. Reliability analysis of connection design based on modified ALPI method

In this section, the modification and implementation of the ALPI method is presented, through which the reliability of the designed bolt axial force demand is assessed. Based on the reliability evaluation, an iterative design improvement procedure is applied, in which an amplification factor is introduced to scale the input design parameters and thereby increase the designed demand until the target reliability index is achieved. This will be detailed in the following subsections.

6.1. Theoretical background of ALPI

Let $\mathbf{X} = [X_1, X_2, \dots, X_d] \in \mathcal{X} \subseteq \mathbb{R}^d$ denotes a vector of d random variables with a known joint probability density function (PDF) $f_{\mathbf{X}}(\mathbf{x})$. Considering the performance function $\mathbf{Y} = g(\mathbf{X}) : \mathcal{X} \rightarrow \mathbf{y}$, the failure event is characterized as $F = \{\mathbf{x} \in \mathcal{X} : g(\mathbf{x}) \leq 0\}$. The corresponding failure probability P_f is defined as follows:

$$P_f = \int_{\mathcal{X}} I(\mathbf{x}) f_{\mathbf{X}}(\mathbf{x}) d\mathbf{x}, \quad (6)$$

where the indicator function $I(\mathbf{x})$ is defined as:

$$I(\mathbf{x}) = \begin{cases} 1, & \text{if } g(\mathbf{x}) \leq 0 \\ 0, & \text{if } g(\mathbf{x}) > 0 \end{cases}. \quad (7)$$

In the ALPI method, $g(\cdot)$ is interpreted as being random in a Bayesian sense as it is numerically unknown until we evaluate it at any given \mathbf{x} . As evaluating $g(\cdot)$ at every possible location is infeasible and impossible, epistemic uncertainty exists wherever $g(\cdot)$ has not been computed. In turn, this kind of uncertainty propagates into the indicator function $I(\mathbf{x})$ and the failure probability estimate. Consequently, the ALPI method is intended to quantify, propagate and reduce the epistemic uncertainty, to estimate the failure probability with fewer evaluations of the computationally expensive performance function.

In ALPI, a prior distribution is first built for $g(\cdot)$, and typically a GP model is adopted. In this context, a GP prior is first placed over $g(\cdot)$ with the prior mean, $m_{g_0}(\mathbf{x})$, and covariance $k_{g_0}(\mathbf{x}, \mathbf{x}')$:

$$\widehat{g}_0 \sim \mathcal{GP}(m_{g_0}(\mathbf{x}), k_{g_0}(\mathbf{x}, \mathbf{x}')), \quad (8)$$

where \widehat{g}_0 denotes the prior distribution of $g(\cdot)$ without conducting any evaluations; $m_{g_0}(\mathbf{x})$ and $k_{g_0}(\mathbf{x}, \mathbf{x}')$ are the prior mean and covariance, respectively. After training the GP model on observations $\mathbf{D} = \{\mathbf{X}_{\text{obs}}, \mathbf{y}\}$ ($\mathbf{X}_{\text{obs}} = \{\mathbf{x}^{(i)}\}_{i=1}^n$ with \mathbf{x} being the i -th row of \mathbf{X}_{obs} , and $\mathbf{y} = \{\mathbf{y}^{(i)}\}_{i=1}^n$ with $\mathbf{y}^{(i)} = g(\mathbf{x}^{(i)})$ being the i th row of \mathbf{y}), and a new GP posterior distribution of $g(\cdot)$ can be obtained:

$$\widehat{g}_n \sim \mathcal{GP}(m_{g_n}(\mathbf{x}), k_{g_n}(\mathbf{x}, \mathbf{x}')), \quad (9)$$

where, the posterior mean and covariance functions are analytically available:

$$m_{g_n}(\mathbf{x}) = m_{g_0}(\mathbf{x}) + \mathbf{k}_{g_0}(\mathbf{x}, \mathbf{X}_{\text{obs}})^T \mathbf{K}_{g_0}^{-1}(\mathbf{y} - m_{g_0}(\mathbf{X}_{\text{obs}})), \quad (10)$$

$$\mathbf{k}_{\hat{g}_n}(\mathbf{x}, \mathbf{x}') = \mathbf{k}_{\hat{g}_0}(\mathbf{x}, \mathbf{x}') - \mathbf{k}_{\hat{g}_0}(\mathbf{x}, \mathbf{X}_{\text{obs}})^T \mathbf{K}_{\hat{g}_0}^{-1} \mathbf{k}_{\hat{g}_0}(\mathbf{X}_{\text{obs}}, \mathbf{x}'), \quad (11)$$

where, $\mathbf{m}_{\hat{g}_0}(\mathbf{X}_{\text{obs}})$ is an $n \times 1$ mean vector, in which the i -th element is $m_{\hat{g}_0}(\mathbf{x}^{(i)})$; $\mathbf{k}_{\hat{g}_0}(\mathbf{x}, \mathbf{X}_{\text{obs}})$ is an $n \times 1$ covariance vector with the i -th entry being $k_{\hat{g}_0}(\mathbf{x}, \mathbf{x}^{(i)})$, and $\mathbf{k}_{\hat{g}_0}(\mathbf{X}_{\text{obs}}, \mathbf{x}')$ is defined in a similar way.

The indicator function $I(\cdot)$ follows a generalized Bernoulli process (GBP), with posterior mean and covariance of \hat{I}_n being $m_{\hat{I}_n}(\mathbf{x})$ and $k_{\hat{I}_n}(\mathbf{x}, \mathbf{x}')$:

$$\hat{I}_n \sim \mathcal{G.B.P.}(m_{\hat{I}_n}(\mathbf{x}), k_{\hat{I}_n}(\mathbf{x}, \mathbf{x}')), \quad (12)$$

and its posterior mean and variance function have analytical expressions:

$$m_{\hat{I}_n}(\mathbf{x}) = \Phi\left(-\frac{m_{\hat{g}_n}(\mathbf{x})}{\sigma_{\hat{g}_n}(\mathbf{x})}\right), \quad (13)$$

$$\sigma_{\hat{I}_n}^2(\mathbf{x}) = \left(-\frac{m_{\hat{g}_n}(\mathbf{x})}{\sigma_{\hat{g}_n}(\mathbf{x})}\right) \Phi\left(\frac{m_{\hat{g}_n}(\mathbf{x})}{\sigma_{\hat{g}_n}(\mathbf{x})}\right), \quad (14)$$

where, Φ is the cumulative distribution function of the standard Gaussian distribution; $\sigma_{\hat{g}_n}(\mathbf{x}) = \sqrt{k_{\hat{g}_n}(\mathbf{x}, \mathbf{x})}$ is the posterior standard deviation of \hat{g}_n .

With Eq. (6), the posterior mean and upper bound of the variance (UPV) of the failure probability P_f (i.e., $\hat{P}_{f, n}$) are available:

$$m_{\hat{P}_{f, n}} = \mathbb{E}_{\hat{I}_n}[\hat{P}_{f, n}] = \int_{\mathcal{X}} \Phi\left(-\frac{m_{\hat{g}_n}(\mathbf{x})}{\sigma_{\hat{g}_n}(\mathbf{x})}\right) f_{\mathbf{X}}(\mathbf{x}) d\mathbf{x}, \quad (15)$$

$$\begin{aligned} \sigma_{\hat{P}_{f, n}}^2 &= \mathbb{V}_{\hat{I}_n}[\hat{P}_{f, n}] \leq \bar{\sigma}_{\hat{P}_{f, n}}^2 \\ &= \left(\int_{\mathcal{X}} \sqrt{\Phi\left(-\frac{m_{\hat{g}_n}(\mathbf{x})}{\sigma_{\hat{g}_n}(\mathbf{x})}\right) \Phi\left(\frac{m_{\hat{g}_n}(\mathbf{x})}{\sigma_{\hat{g}_n}(\mathbf{x})}\right)} f_{\mathbf{X}}(\mathbf{x}) d\mathbf{x} \right)^2, \end{aligned} \quad (16)$$

where, $\mathbb{E}_{\hat{I}_n}[\cdot]$ and $\mathbb{V}_{\hat{I}_n}[\cdot]$ are the expectation and variance operators taken over \hat{I}_n , respectively, and $\bar{\sigma}_{\hat{P}_{f, n}}^2$ is the UPV of $\hat{P}_{f, n}$.

6.2. Numerical algorithm

The ALPI method is employed to estimate the failure probability using as few performance function evaluations as possible, without compromising accuracy. Given that no closed-form solutions exist for Eqs. (15) and (16), the Monte Carlo simulation is employed to calculate the failure probability estimate and prediction uncertainty, and the original algorithm is illustrated below:

Step 1: Generate a Monte Carlo population of N_{mcs} samples according to $f_{\mathbf{X}}(\mathbf{x})$, denoted by $\overline{\mathbf{X}}_{\text{obs}} = \{\overline{\mathbf{x}}^{(i)}\}_{i=1}^{N_{\text{mcs}}}$.

Step 2: Randomly select N_0 ($N_0 = 10$ is adopted herein) points among the sample population, which will be evaluated on the performance function $g(\cdot)$ to get corresponding observations, and in turn form the initial dataset \mathbf{D} .

Step 3: Train the GP model based on the data \mathbf{D} , and calculate the posterior mean of failure probability:

$$\tilde{m}_{\hat{P}_{f, n}} = \frac{1}{N_{\text{mcs}}} \sum_{i=1}^{N_{\text{mcs}}} \Phi\left(-\frac{m_{\hat{g}_n}(\overline{\mathbf{x}}^{(i)})}{\sigma_{\hat{g}_n}(\overline{\mathbf{x}}^{(i)})}\right), \quad (17)$$

and the upper-bound of posterior standard deviation:

$$\tilde{\sigma}_{\hat{P}_{f, n}} = \frac{1}{N_{\text{mcs}}} \sum_{i=1}^{N_{\text{mcs}}} \sqrt{\Phi\left(-\frac{m_{\hat{g}_n}(\overline{\mathbf{x}}^{(i)})}{\sigma_{\hat{g}_n}(\overline{\mathbf{x}}^{(i)})}\right) \Phi\left(\frac{m_{\hat{g}_n}(\overline{\mathbf{x}}^{(i)})}{\sigma_{\hat{g}_n}(\overline{\mathbf{x}}^{(i)})}\right)}, \quad (18)$$

Step 4: Check the stopping criterion, the estimated upper bound of posterior coefficient of variation (CoV) of the failure probability. If $\text{CoV} = \tilde{\sigma}_{\hat{P}_{f, n}} / \tilde{m}_{\hat{P}_{f, n}} < \epsilon$ is satisfied, where $\epsilon = 0.15$ is adopted herein, go to

Step 6. Else, go to **Step 5.**

Step 5: Enrich \mathbf{D} by selecting the best next point to be evaluated on the g -function through a learning function called upper-bound posterior variance contribution (UPVC):

$$\text{UPVC}(\overline{\mathbf{x}}^{(i)}) = \sqrt{\Phi\left(-\frac{m_{\hat{g}_n}(\overline{\mathbf{x}}^{(i)})}{\sigma_{\hat{g}_n}(\overline{\mathbf{x}}^{(i)})}\right) \Phi\left(\frac{m_{\hat{g}_n}(\overline{\mathbf{x}}^{(i)})}{\sigma_{\hat{g}_n}(\overline{\mathbf{x}}^{(i)})}\right)} f_{\mathbf{X}}(\overline{\mathbf{x}}^{(i)}), \quad (19)$$

in which the best next point \mathbf{x}^* satisfies that $\mathbf{x}^* = \arg \max_{\overline{\mathbf{x}} \in \overline{\mathbf{X}}_{\text{obs}}} \text{UPVC}(\overline{\mathbf{x}})$.

Accordingly, the dataset \mathbf{D} is enriched by $\mathbf{D} = \mathbf{D} \cup \{g(\mathbf{x}^*)\}$. Go to **Step 3.**

Step 6: Return $\tilde{m}_{\hat{P}_{f, n}}$ as the estimated failure probability.

6.3. Modifications of ALPI method and implementation

As progressive collapse of building structures generally leads to catastrophic consequences, warranting high priority in structural design, a target design reliability greater than 4.2 is recommended, specified in the Chinese design code for structural design reliability [45]. Achieving such a high level of reliability necessitates the evaluation of small failure probabilities, which would require an extremely large Monte Carlo sample population. In this regard, selecting the best next point \mathbf{x}^* in the candidate population imposes a significant computational burden during the active learning procedure. Therefore, a new strategy based on an optimization approach is adopted, wherein the Starfish Optimization Algorithm (SFOA) [46] is employed within the numerical framework to efficiently identify \mathbf{x}^* within clearly defined search boundaries.

In addition, a modification for the learning function, UPVC, is introduced to adapt the ALPI method to the current strongly nonlinear structural collapse problem. This modification is motivated by the observation that, while it is important to select points that reduce the upper bound of the posterior variance, overly dense sampling in localized regions can hinder the GP model to capture strong nonlinear behavior. To address this, the original learning function is multiplied by $\sigma_{\hat{g}_n}(\mathbf{x})$, the prediction uncertainty of the GP model, which serves as a penalty term. As the predictive uncertainty in GP models diminishes near training points, this penalization discourages point selection in already well-explored areas. Building upon this idea, increasing the exponent of $\sigma_{\hat{g}_n}(\mathbf{x})$ from one to higher values expands the penalized region, thereby promoting a more diverse distribution of selected points during the active learning procedure. This strategy enables the convergence of the upper bound of the posterior CoV toward a predefined criterion. By trial and error, an exponent of 6 is determined to be effective for the current problem. This modified learning function is therefore referred to as penalty-adjusted upper-bound posterior variance contribution (PUPVC):

$$\text{PUPVC}(\mathbf{x}) = \sigma_{\hat{g}_n}^6(\mathbf{x}) \sqrt{\Phi\left(-\frac{m_{\hat{g}_n}(\mathbf{x})}{\sigma_{\hat{g}_n}(\mathbf{x})}\right) \Phi\left(\frac{m_{\hat{g}_n}(\mathbf{x})}{\sigma_{\hat{g}_n}(\mathbf{x})}\right)} f_{\mathbf{X}}(\mathbf{x}). \quad (20)$$

The reliability assessment algorithm is then implemented in MATLAB (2024a), which offers built-in `fitrgp` function that provides flexible customization of GP models and post-processing of the fitted results. In specific, a constant mean and the 'ardmatern52' kernel is selected that adapts for fitting nonlinear problems:

$$k_{\text{ardmatern5/2}}(\mathbf{x}_i, \mathbf{x}_j | \boldsymbol{\alpha}) = \sigma_f^2 \left(1 + \sqrt{5} r_{ij} + \frac{5}{3} r_{ij}^2\right) \exp\left(-\sqrt{5} r_{ij}\right), \quad (21)$$

$$r_{ij} = \sqrt{\sum_{m=1}^d \frac{(x_{i, m} - x_{j, m})^2}{\ell_m^2}}, \quad (22)$$

where $\mathbf{x}_i, \mathbf{x}_j \in \mathbb{R}^d$ are two input vectors; σ_f^2 is the marginal signal vari-

ance; $\ell_m > 0$ is the length-scale for the m -th input dimension; and $\alpha = (\sigma_f, \ell_1, \ell_2, \dots, \ell_d)$ collects all hyper-parameters.

In addition, considering the physical constraint that the rebar yield strength must be smaller than the ultimate strength (see Section 6.4), a penalty option is additionally included in searching \mathbf{x}^* using SFOA:

$$I_c(\mathbf{x}) = \begin{cases} 1, & \text{if } x_y > x_u \\ 0, & \text{if } x_y \leq x_u \end{cases}, \quad (23)$$

$$F_{\text{tbo}}(\mathbf{x}) = -\text{PUPVC}(\mathbf{x}) + I_c(\mathbf{x}) \times 10^8, \quad (24)$$

where, $I_c(\mathbf{x})$ is an indicator function that equals to one only when the yield strength x_y is greater than the ultimate strength x_u . To effectively prevent candidates violating the physical constraint from being selected, a significantly large constant is added to the objective function value, F_{tbo} , to reduce their selection probability (see Eq. (24)).

6.4. Consideration of the uncertainties

In engineering practice, geometric uncertainties arising from construction processes and material property variations are widespread [15,18,20,21]. However, the geometric uncertainties in PC frame structures are difficult to quantify due to limited field data. Furthermore, the effects of such uncertainties on joint behavior are difficult to capture using a simplified FE model. Therefore, in this study, only uncertainties in critical material properties that result in variability in bolt force demand are included in the reliability assessment, as tabulated in Table 1. Moreover, the concrete compressive strength and concrete peak strain are statistically dependent. This dependence is modeled using a 90° Clayton copula ($\rho_{12} = 0.9411$), as experimentally explored by Tao et al. [47]. On the other hand, the probabilistic dependence between the concrete tensile strength and compressive strength has not been established. Accordingly, a deterministic relationship between the two is adopted here, as suggested by Lyu et al. [48]. In addition, the commonly adopted statistical distributions for rebar yield and ultimate strengths overlap, which might lead to physically meaningless combinations in which the yield strength exceeds the ultimate strength. Therefore, a sample-rejection iteration is incorporated within the Monte Carlo sampling process till the full sample population satisfied the required condition.

6.5. Reliability assessment and design update results

In this case, the performance function $g(\cdot)$ is defined as:

$$g(\mathbf{x}) = F_{\text{UB}}(af_u) - F_{\text{REAL}}(\mathbf{x}) \quad (25)$$

where \mathbf{x} represents the parameters involving uncertainties considered herein, as listed in Table 1; F_{UB} is the designed bolt axial demand, and F_{REAL} is the maximum bolt axial force calculated from the simplified FE model considering uncertainties.

It should be noted that, in progressive collapse problems, the uncertainty in the initiating action is difficult to quantify probabilistically in a unified manner. This is mainly due to two aspects: (1) various accidental extreme events may lead to progressive collapse (e.g.,

explosion, vehicle impact, and terrorist attacks), and their hazard characteristics and intensity measures differ significantly, making it difficult to construct a consistent probabilistic load model; (2) even for a specific accidental event, the available data are usually scarce, which prevents establishing a statistically reliable probability distribution for the corresponding action and damage level [20]. Therefore, consistent with most published progressive collapse studies [18–21], the accidental action is commonly represented by a predefined scenario and a prescribed demand level, rather than being explicitly treated as a random variable.

In this study, the progressive collapse demand is regulated by a displacement-controlled analysis with a prescribed deformation level (MJD = 600 mm). The maximum bolt axial force $F_{\text{REAL}}(\mathbf{x})$ is extracted from the response history under this prescribed deformation path. Accordingly, the reported failure probability (or reliability index) should be interpreted as conditional on the specified collapse scenario and deformation demand (MJD = 600 mm), while the uncertainties are considered in the structural parameters \mathbf{x} listed in Table 1.

The mean value of f_u is initially selected as the input design parameter to provide a statistically representative baseline to derive F_{UB} . An amplification factor, a , is multiplied to F_u to adjust the designed bolt axial force demand when the reliability is not satisfied. The performance function implies that failure occurs once F_{REAL} exceeds the precalculated upper bound F_{UB} . Finally, by integrating the design method (Section 3), the simplified FE model (Section 4), and the modified ALPI method (this section), the design reliability is assessed. After each reliability assessment, the value of a is gradually increased until the target reliability index $\beta_t = 4.2$ is surpassed. The results of reliability assessment are illustrated in Table 2. A final value of $a = 1.08$ is determined, yielding a reliability index of 4.36, which satisfies the design target.

To summarize, when integrated with the deterministic design and the simplified FE model, this reliability assessment completes the proposed framework for a computationally efficient and reliability-aware collapse-resisting design of precast concrete beam–column joint using strengthened steel angles and high-strength bolts.

7. Global sensitivity analysis and reliability sensitivity analysis

Even after demonstrating that the proposed design method achieves the target reliability, it is essential to trace how the input uncertainties and modelling choices propagate through the performance function, in terms of both output variance and failure probability. It is noted that progressive collapse develops through multiple stages with different resistance mechanisms (Fig. 15), and the sensitivity of influencing parameters may vary from stage to stage. However, the present study targets the bolt design demand, and the bolt axial force in the final collapse state is markedly larger than that in earlier stages, as shown in Fig. 7. Therefore, the following sensitivity analyses are formulated with respect to the maximum bolt axial force at the final progressive collapse state (MJD = 600 mm). To this end, a variance-based Sobol global sensitivity analysis (GSA) is conducted to rank each input contribution to response scatter, and a GP model post-processing-based reliability sensitivity analysis (RSA) is performed to quantify each variable's influence on the achieved design reliability.

Table 1
Distribution information.

Material properties	Mean	CoV	Distribution
Concrete compressive strength (MPa, f_c)	27	0.1619	Lognormal [47]
Concrete peak strain (ϵ_c)	0.0018	0.1371	Gamma [47]
Rebar elastic modulus (GPa, E_s)	200	0.033	(truncated) Normal [15]
Rebar yield strength (MPa, f_y)	337	0.107	Beta [49]
Rebar ultimate strength (MPa, f_u)	517	0.107	Beta [49]
Rebar fracture strain (ϵ_s)	0.12	0.15	Lognormal [15]

Table 2
Reliability assessment results.

Iteration	a	Failure probability, P_f	Resulting reliability index, β_r	Target reliability index, β_t
0	1	0.0013	3.00	4.2
1	1.05	7.3036×10^{-5}	3.80	
2	1.07	1.5912×10^{-5}	4.16	
3	1.08	5.9464×10^{-6}	4.38	

7.1. Sobol's variance-based GSA

GSA is performed to rank the influence of all six input parameters on the output variance. Let $Y = g(\mathbf{X})$ denotes the performance function response, where $\mathbf{X} = (X_1, \dots, X_6)$. The total variance can be decomposed into contributions from individual inputs and their interactions. The corresponding Sobol' indices are defined as:

$$S_i = \frac{\text{Var}(\mathbb{E}[Y|X_i])}{\text{Var}(Y)}, \quad (26)$$

$$S_{ij} = \frac{\text{Var}(\mathbb{E}[Y|X_i, X_j]) - \text{Var}(\mathbb{E}[Y|X_i]) - \text{Var}(\mathbb{E}[Y|X_j])}{\text{Var}(Y)}, i \neq j, \quad (27)$$

$$S_{T_i} = 1 - \frac{\text{Var}(\mathbb{E}[Y|\mathbf{X}_{-i}])}{\text{Var}(Y)} = \frac{\mathbb{E}[\text{Var}(Y|\mathbf{X}_{-i})]}{\text{Var}(Y)}, \quad (28)$$

where S_i , S_{ij} , and S_{T_i} are the first-order, second-order, and total-effect indices, respectively; \mathbf{X}_{-i} denotes the set of all inputs except X_i . The GP model obtained from previous reliability analysis is adopted to evaluate the performance function for each Sobol's quasi-random sample, mapped through the prescribed input distributions and copula in UQLab [50]. The sample size is gradually increased until the results converged, and the final size is 1×10^5 .

The Sobol's sensitivity results are displayed in Fig. 16. They reveal a clear hierarchy among the six input uncertainties, which shows that the first-order and total-order indices of the concrete properties (f_c and ϵ_c) and the rebar elastic modulus (E_s) are essentially zero, and that all pairwise interaction indices are below 3.5×10^{-3} . This confirms that under extreme collapse scenarios these three inputs have a negligible influence on the variance of the bolt axial force, in line with earlier local sensitivity studies [16,21]. By contrast, the rebar ultimate strength (f_u) and fracture strain (ϵ_s) dominate the output variance: their first-order indices are 0.42 and 0.49, and their total-order indices are 0.50 and 0.51, respectively, together accounting for essentially 100% of the variance when interactions are included. In addition, the rebar yield strength (f_y) has a nonzero total-order index (0.07), but this is still an order of magnitude smaller than those of f_u and ϵ_s , indicating its influence is negligible in comparison.

7.2. GP model post-processing-based RSA

Although GSA analysis ranks the high-impact variables in terms of structural response, their effects on reliability may differ due to potential tail influence. Therefore, RSA is performed on the mean (μ) and standard deviation (σ) of each random variable. Using the trained GP model, the

sensitivity of the estimated failure probability $m_{p_{f,n}}$, with respect to μ and σ of the input variables can be expressed as:

$$\frac{\partial m_{p_{f,n}}}{\partial \gamma_{l,i}} = \int_{\mathcal{X}} \Phi \left(-\frac{m_{g_n}(\mathbf{x})}{\sigma_{g_n}(\mathbf{x})} \right) \frac{\partial f_{\mathbf{x}}(\mathbf{x}; \boldsymbol{\gamma})}{\partial \gamma_{l,i}} d\mathbf{x}, \quad (29)$$

where, $\boldsymbol{\gamma}$ and $\gamma_{l,i}$ represent the collection of all distribution parameters and the i -th distribution parameter (e.g. mean or standard deviation) of the l -th input, respectively. To simplify the numerical computation, the likelihood ratio method is applied [51,52]:

$$\frac{\partial f_{\mathbf{x}}(\mathbf{x}; \boldsymbol{\gamma})}{\partial \gamma_{l,i}} = \frac{\partial \ln f_{\mathbf{x}}(\mathbf{x}; \boldsymbol{\gamma})}{\partial \gamma_{l,i}} f_{\mathbf{x}}(\mathbf{x}; \boldsymbol{\gamma}), \quad (30-1)$$

and it yields:

$$\frac{\partial m_{p_{f,n}}}{\partial \gamma_{l,i}} = \int_{\mathcal{X}} \Phi \left(-\frac{m_{g_n}(\mathbf{x})}{\sigma_{g_n}(\mathbf{x})} \right) \frac{\partial \ln f_{\mathbf{x}}(\mathbf{x}; \boldsymbol{\gamma})}{\partial \gamma_{l,i}} f_{\mathbf{x}}(\mathbf{x}; \boldsymbol{\gamma}) d\mathbf{x}, \quad (30-2)$$

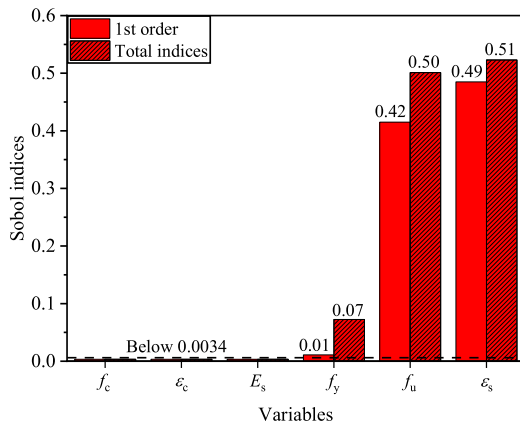
where, the likelihood ratio for each distribution is provided in Appendix B. This enables a practical Monte Carlo-based estimation:

$$\widehat{\frac{\partial m_{p_{f,n}}}{\partial \gamma_{l,i}}} = \frac{1}{N_{\text{mc}}} \sum_{j=1}^{N_{\text{mc}}} \Phi \left(-\frac{m_{g_n}(\bar{\mathbf{x}}^{(j)})}{\sigma_{g_n}(\bar{\mathbf{x}}^{(j)})} \right) \frac{\partial \ln f_{\mathbf{x}}(\bar{\mathbf{x}}^{(j)}; \boldsymbol{\gamma})}{\partial \gamma_{l,i}}, \quad (31)$$

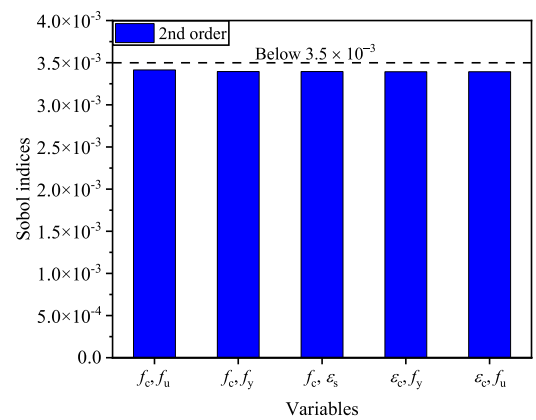
where, the corresponding sample population is reused to improve computational efficiency. To eliminate the effect of variable magnitude to present a meaningful comparison across inputs, the sensitivity results are transformed into elasticity forms. Elasticities are dimensionless measures that capture the relative impact of distribution parameter on the failure probability, allowing for consistent and interpretable evaluation of parameter importance [53]:

$$\epsilon_{\gamma_{l,i}} = \frac{\gamma_{l,i}}{m_{p_{f,n}}} \frac{\partial \widehat{m_{p_{f,n}}}}{\partial \gamma_{l,i}}. \quad (32)$$

The elasticity-based reliability sensitivities to the key distribution parameters are shown in Fig. 17, where a positive elasticity $\epsilon_{\gamma_{l,i}}$ indicates that a 1% increase in the parameter increases the failure probability by $\epsilon_{\gamma_{l,i}}$ %, and vice versa for a negative value. For the most part, RSA yields results consistent with GSA: the concrete material properties and the rebar elastic modulus have negligible influence on the design reliability; whereas the influences of f_u and ϵ_s are still high. By contrast, f_y plays a different but significant role in affecting the reliability, even higher than that of ϵ_s . More specifically, the mean values of f_u , f_y , and ϵ_s are the most influential variables, with elasticities of 29.24, 21.34, and



(a) 1st order Sobol sensitivity indices



(b) 2nd order Sobol sensitivity indices

Fig. 16. Global sensitivity analysis results.

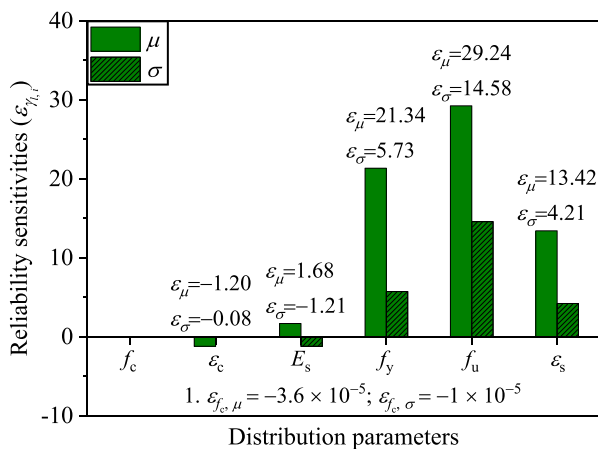


Fig. 17. Elasticity-based reliability sensitivities.

13.42, respectively, and the elasticities with respect to their σ values are 14.58, 5.73, and 4.21, respectively, indicating that increases in these variables can markedly increase the failure probability under the prescribed design demand.

In general, the RSA results suggest that in the design phase, f_u , f_y , and ϵ_s should be carefully handled. From a manufacturing perspective, stringent rebar quality control should be ensured to reduce the failure probability of the joint connection under the prescribed design demand. However, in the present study, only f_u is considered in the design phase, as it is the variable most directly affecting the extreme structural response. While quantifying the effects of f_y and ϵ_s on joint demand requires an accurate analysis of the entire collapse-evolution analysis, it remains a challenging problem.

In summary, both GSA and RSA enable effective identification of the critical random variables governing the structural response variance and design reliability, and these complementary methods ensure that the potential tail effect of f_y , which has a limited impact on variance, is not overlooked. Furthermore, the integration of the trained GP model with Sobol' indices and the likelihood ratio method provides a highly efficient framework for performing sensitivity analysis in complex structural analysis.

8. Conclusion

This study proposes a reliability-aware design framework for dry beam-column connections using strengthened steel angles and high-strength bolts. A deterministic design is established through configuration optimization and identification of load transfer mechanisms based on a detailed FE model, leading to an analytical upper-bound estimate of column bolt axial force as the design target. By resorting to a developed simplified FE model and the tailored ALPI method, the design reliability is efficiently assessed and enhanced conditional on the specified collapse scenario and deformation demand (MJD = 600 mm), under strong nonlinearities and rare-event conditions. Finally, by integrating the trained GP model in ALPI with Sobol' indices and the likelihood ratio method, both GSA and RSA are performed. On this basis, the following specific conclusions can be drawn:

- (1) Through LS-DYNA, a detailed FE model that simulates structural progressive collapse is established and validated for the beam-column assembly using the dry connection composed of strengthened steel angles and high-strength bolts. Based on the FE model, it is identified that CL can induce higher joint capacity demand compared to UDL in engineering practice. Under the CL condition, a steel angle configuration optimization is performed to avoid undesired bolt failure modes, and the load transfer

mechanisms are identified and validated with 1% error. Accordingly, this enables an efficient and practical collapse resisting design for the joint connection focusing on the column bolt axial force demand, for which the upper bound is derived based on the ultimate strength of the beam rebar.

- (2) Based on the validated load transfer mechanisms within the joint region, a macro joint model is developed using beam elements and spring elements that captures the connection behavior. Combining with the fiber beam elements, a simplified FE model is formed and validated that can accurately predict the overall collapse resistance and the ultimate column bolt axial force, providing fast model evaluations in reliability analysis while preserving prediction accuracy.
- (3) The ALPI method is employed for assessing the connection design reliability due to its highly efficient reliability assessment using a small number of model evaluations. The learning function and point selection strategy are modified to select the most informative and also diverse evaluation points, by multiplying the posterior prediction by a variance-related term, and $\sigma_{g_n}(\mathbf{x})^6$ is determined to achieve the best learning performance. Besides, SFOA is employed to efficiently identify the best next point to avoid the estimation of each candidate point and ensure a clear search boundary.
- (4) As the connected structural components are the main sources of the joint connection demand, the uncertainties in their material properties are considered in this study. An amplification factor for the rebar ultimate strength is determined as 1.08 yielding a design reliability index of 4.38, which is greater than the 4.2 stipulated in the design regulation. In addition, by integrating the GP model trained in ALPI with Sobol' indices and the likelihood ratio method, a highly efficient framework for performing GSA and RSA in complex structural analysis is established. GSA indicates that f_u and ϵ_s essentially control the variance of the ultimate bolt force, while RSA highlights that f_y also has a significant impact on the design reliability ranked between f_u and ϵ_s . The reliability sensitivities in elasticity form are 29.24, 21.34, and 13.42, and 14.58, 5.73, and 4.21, respectively, for their respective means (μ) and standard deviations (σ). This emphasizes the need to further consider f_y and ϵ_s in future design analyses. Besides, tighter quality control on the rebar is recommended to improve the design reliability.
- (5) The main objective of this study is to propose a foundational yet complete framework for the collapse-resisting design of a specific type of dry connection joint. This includes internal force analysis, design methodology, macro joint model development, and high-efficient reliability and sensitivity assessment. The framework remains open for further refinements, such as: 1) improving design updating incorporating f_y and ϵ_s ; 2) considering geometric nonlinearities in the simplified model or adopting reliability methods capable of handling fuzzy probability distributions in the presence of limited data; and so on.

CRedit authorship contribution statement

Zidong Zhao: Writing – review & editing, Writing – original draft, Visualization, Validation, Software, Methodology, Investigation, Formal analysis, Conceptualization. **Marcos A. Valdebenito:** Writing – review & editing, Supervision, Methodology, Conceptualization. **Yi Li:** Writing – review & editing, Supervision, Project administration, Methodology, Funding acquisition, Conceptualization. **Chao Dang:** Writing – review & editing, Supervision, Software, Methodology, Investigation, Conceptualization. **Weijing Zhang:** Writing – review & editing, Validation, Supervision. **Matthias G.R. Faes:** Writing – review & editing, Supervision, Methodology, Funding acquisition, Conceptualization.

Declaration of competing interest

The authors declare that they have no known competing financial interests or personal relationships that could have appeared to influence the work reported in this paper.

Acknowledgement

Zidong Zhao and Yi Li are grateful for the financial support received from the National Natural Science Foundation of China (No. 52178094). Zidong Zhao also acknowledges the support received from China Scholar Council (CSC). Chao Dang is grateful for the financial support of the German Research Foundation (DFG) (Grant457 number 530326817).

Appendix A. FE model information

A.1. Detailed FE model information

A.1.1. Element types and material models

The solid elements adopted are 8-node solid elements with reduced (single-integration) point, while the beam elements adopted are 2-node Hughes-Liu beam elements with 2×2 Gauss quadrature integration. The keyword *CONSTRAINED_BEAM_IN_SOLID (*CBIS) is employed for building the interaction between concrete and rebars. The continuous surface cap model (*MAT_159/*MAT_CSCM) in LS-DYNA is adopted to represent concrete in progressive collapse. This is because it can consider damage-driven softening, shear dilation/compaction, and confinement-dependent response [30,39,40], which are important for simulating the concrete behavior under extreme collapse state. In LS-DYNA, model parameters defining for concrete with uniaxial compression strengths ranging from 28 to 48 MPa can be generated internally by the model. The corresponding setting adopted in this research is displayed in Fig. A1, followed by its uniaxial response shown in Fig. A2. The piecewise linear plastic model (*MAT_024/*MAT_PIECEWISE_LINEAR_PLASTICITY) in LS-DYNA is utilized to represent rebars and steel components. Both material models simulate failure scenario based on strain criteria. *MAT_159 defines concrete failure by the maximum principal strain (ϵ_{max}), which is set to 0.1 in accordance with the recommendation of Pham et. al [40]. *MAT_024 takes specific effective plastic strain (ϵ_{eff}) values to control the failure of each steel component.

*MAT_CSCM_(TITLE) (159) (1)								
<u>TITLE</u>								
<input type="text"/>								
1	<u>MID</u>	<u>RO</u>	<u>NPLOT</u>	<u>INCRE</u>	<u>IRATE</u>	<u>ERODE</u>	<u>RECOV</u>	<u>ITRETRC</u>
	1	2.400e-09	1	0.0	0	1.1000000	0.0	0
2	<u>PRED</u>							
	0.0							
3	<u>G</u>	<u>K</u>	<u>ALPHA</u>	<u>THETA</u>	<u>LAMDA</u>	<u>BETA</u>	<u>NH</u>	<u>CH</u>
	1.194e+04	1.308e+04	15.000000	0.3092000	10.510000	0.0192900	0.0	0.0
4	<u>ALPHA1</u>	<u>THETA1</u>	<u>LAMDA1</u>	<u>BETA1</u>	<u>ALPHA2</u>	<u>THETA2</u>	<u>LAMDA2</u>	<u>BETA2</u>
	0.7473000	0.0010420	0.1700000	0.0664000	0.6600000	0.0012560	0.1600000	0.0664000
5	<u>R</u>	<u>XD</u>	<u>W</u>	<u>D1</u>	<u>D2</u>			
	5.0000000	92.480003	0.0500000	2.500e-04	3.492e-07			
6	<u>B</u>	<u>GFC</u>	<u>D</u>	<u>GFI</u>	<u>GFS</u>	<u>PWRC</u>	<u>PWRT</u>	<u>PMOD</u>
	100.000000	6.1910000	0.1000000	0.0619100	0.0619100	5.0000000	1.0000000	0.0
7	<u>ETA0C</u>	<u>NC</u>	<u>ETA0T</u>	<u>NT</u>	<u>OVERC</u>	<u>OVERT</u>	<u>SRATE</u>	<u>REP0W</u>
	1.075e-04	0.7800000	6.550e-05	0.4800000	23.219999	23.219999	1.0000000	1.0000000

Fig. A.1. Parameter definitions of CSCM in LS-DYNA.

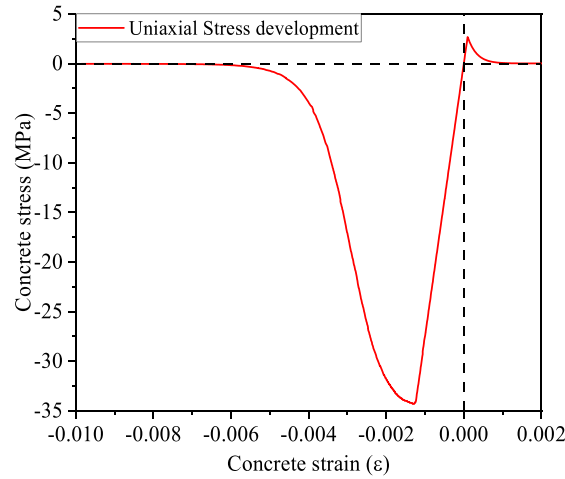


Fig. A.2. Uniaxial response of CSCM in LS-DYNA.

A.1.2. Boundary conditions

In the test, the gap between the constraints and the assembly was reported [29]. It is finally considered at bottom of the column calibrated with iterative result comparisons, which allows the column to displace outward by up to 4 mm. In addition, out-of-plane constraints are implemented by constraining the translational degree of freedom in y-axis of the beam. All contacts among the steel components, and between the steel components and concrete parts are considered by the keyword *CONTACT_AUTOMATIC_SURFACE_TO_SURFACE (*CASTS) for solid elements.

A.1.3. Joint details

The joint connection is fully replicated according to construction details. The contacts among different steel components established using solid elements are defined using *CASTS, while the contacts among bolts built with beam elements and surrounding components (solid elements) are considered through the keyword *CONTACT_BEAM_TO_SURFACE. At the beam ends, the rebar ends are embedded into steel plate regions with perfect bonding conditions by *CBIS to simulate the weld anchorage.

A.2. Details of simplified model establishment

The boundary elements in the simplified model is modelled using *MAT_024, namely the piecewise linear plastic model, whereas the rigid beam end is modelled using the material model *MAT_020/MAT_RIGID. In addition, LS-DYNA regulates that the fiber beam elements should adopt identical material model for each integration point in the section. Therefore, the material model *MAT_174/MAT_RC_BEAM is adopted, as it can simulate both concrete and rebar behavior by adjusting the parameter of FRACR, for which, 0 corresponds to pure concrete, and 1 corresponds to pure rebars. And the keyword *INTEGRATION_BEAM enables assigning the integrations for different materials. And single rebar fiber failure is realized by considering an additional keyword *MAT_000/MAT_ADD_EROSION in combination with *MAT_174. Once the rebar axial stress corresponding to a defined fracture strain is reached, the fiber part is deleted.

Appendix B. Likelihood ratio derivative

B.1. Partial derivative of the likelihood ratio of the beta distribution to mean, μ_m and standard deviation, σ_m

In this study, the probability density distribution (PDF) of the rebar ultimate strength follows a beta distribution:

$$f(x) = \frac{1}{aB(\alpha, \beta)} \left(\frac{x-b}{a}\right)^{\alpha-1} \left(\frac{a+b-x}{a}\right)^{\beta-1}, \quad (\text{B.1-1})$$

where, $B(\alpha, \beta) = \Gamma(\alpha)\Gamma(\beta)/\Gamma(\alpha + \beta)$, with α and β being 3.21 and 4.82; b and $b+a$ determine the distribution interval [55, 105] in Psi. The partial derivatives for $\ln f(x)$ with respect to μ_m and σ_m , the real mean and standard deviation of the transformed beta distribution, are derived as following, and to keep the notation compact and the logic clear, a few intermediate quantities are introduced with separate explanations:

$$\frac{\partial \ln f}{\partial \alpha} = \ln \frac{x-b}{a} - [\psi(\alpha) - \psi(\alpha + \beta)] = A(x), \quad (\text{B.1-2})$$

$$\frac{\partial \ln f}{\partial \beta} = \ln \frac{a+b-x}{a} - [\psi(\beta) - \psi(\alpha + \beta)] = B(x), \quad (\text{B.1-3})$$

$$\frac{\partial \alpha}{\partial \mu_m} = \frac{\partial \alpha}{\partial \mu} \frac{\partial \mu}{\partial \mu_m} = \left(C + \frac{\mu(1-2\mu)}{\sigma^2}\right) \frac{\partial \mu}{\partial \mu_m}, \quad (\text{B.1-4})$$

$$\frac{\partial \beta}{\partial \mu_m} = \frac{\partial \beta}{\partial \mu} \frac{\partial \mu}{\partial \mu_m} = \left(-C + \frac{(1-\mu)(1-2\mu)}{\sigma^2}\right) \frac{\partial \mu}{\partial \mu_m}, \quad (\text{B.1-5})$$

$$\frac{\partial \alpha}{\partial \sigma_m} = \frac{\partial \alpha}{\partial \sigma} \frac{\partial \sigma}{\partial \sigma_m} = -2 \frac{\mu^2(1-\mu)}{\sigma^3} \frac{\partial \sigma}{\partial \sigma_m}, \tag{B.1-6}$$

$$\frac{\partial \beta}{\partial \sigma_m} = \frac{\partial \beta}{\partial \sigma} \frac{\partial \sigma}{\partial \sigma_m} = -2 \frac{\mu(1-\mu)^2}{\sigma^3} \frac{\partial \sigma}{\partial \sigma_m}, \tag{B.1-7}$$

$$\begin{aligned} \frac{\partial \ln f}{\partial \mu_m} &= \frac{\partial \ln f}{\partial \alpha} \frac{\partial \alpha}{\partial \mu} \frac{\partial \mu}{\partial \mu_m} + \frac{\partial \ln f}{\partial \beta} \frac{\partial \beta}{\partial \mu} \frac{\partial \mu}{\partial \mu_m} \\ &= A(x) \left[C \frac{\partial \mu}{\partial \mu_m} + \frac{\mu(1-2\mu)}{\sigma^2} \frac{\partial \mu}{\partial \mu_m} \right] + B(x) \left[-C \frac{\partial \mu}{\partial \mu_m} + \frac{(1-\mu)(1-2\mu)}{\sigma^2} \frac{\partial \mu}{\partial \mu_m} \right], \end{aligned} \tag{B.1-8}$$

$$\begin{aligned} \frac{\partial \ln f}{\partial \sigma_m} &= \frac{\partial \ln f}{\partial \alpha} \frac{\partial \alpha}{\partial \sigma} \frac{\partial \sigma}{\partial \sigma_m} + \frac{\partial \ln f}{\partial \beta} \frac{\partial \beta}{\partial \sigma} \frac{\partial \sigma}{\partial \sigma_m} \\ &= A(x) \left[-2 \frac{\mu^2(1-\mu)}{\sigma^3} \frac{\partial \sigma}{\partial \sigma_m} \right] + B(x) \left[-2 \frac{\mu(1-\mu)^2}{\sigma^3} \frac{\partial \sigma}{\partial \sigma_m} \right], \end{aligned} \tag{B.1-9}$$

where, $C = \mu(1-\mu)/\sigma^2 - 1$; $\partial \mu / \partial \mu_m = \partial \sigma / \partial \sigma_m = 1/a$ and $\psi(\bullet)$ is the digamma function, the logarithmic derivative of the Gamma function, $\Gamma(\bullet)$.

B.2. Partial derivative of the likelihood ratio of the lognormal distribution to μ_m and σ_m

The PDF of the rebar fracture strain follows a lognormal distribution:

$$f(x) = \frac{1}{x\sigma\sqrt{2\pi}} \exp \left[-\frac{(\ln x - \mu)^2}{2\sigma^2} \right], x > 0, \tag{B.2-1}$$

where, μ and σ are the mean and standard deviation of $\ln x$. The partial derivatives for $\ln f(x)$ with respect to μ_m and σ_m are derived as following:

$$\frac{\partial \ln f}{\partial \mu} = \frac{\ln x - \mu}{\sigma^2}, \tag{B.2-2}$$

$$\frac{\partial \ln f}{\partial \sigma} = -\frac{1}{\sigma} + \frac{(\ln x - \mu)^2}{\sigma^3}, \tag{B.2-3}$$

$$\frac{\partial \mu}{\partial \mu_m} = \frac{\mu_m^2 + 2\sigma_m^2}{\mu_m(\mu_m^2 + \sigma_m^2)}, \tag{B.2-4}$$

$$\frac{\partial \mu}{\partial \sigma_m} = -\frac{\sigma_m}{\mu_m^2 + \sigma_m^2}, \tag{B.2-5}$$

$$\frac{\partial \sigma}{\partial \mu_m} = -\frac{\sigma_m^2}{\sigma \mu_m(\mu_m^2 + \sigma_m^2)}, \tag{B.2-6}$$

$$\frac{\partial \sigma}{\partial \sigma_m} = \frac{\sigma_m}{\sigma(\mu_m^2 + \sigma_m^2)}, \tag{B.2-7}$$

$$\begin{aligned} \frac{\partial \ln f}{\partial \mu_m} &= \frac{\partial \ln f}{\partial \mu} \frac{\partial \mu}{\partial \mu_m} + \frac{\partial \ln f}{\partial \sigma} \frac{\partial \sigma}{\partial \mu_m} \\ &= \frac{\ln x - \mu}{\sigma^2} \frac{\mu_m^2 + 2\sigma_m^2}{\mu_m(\mu_m^2 + \sigma_m^2)} + \left(-\frac{1}{\sigma} + \frac{(\ln x - \mu)^2}{\sigma^3} \right) \left(-\frac{\sigma_m^2}{\sigma \mu_m(\mu_m^2 + \sigma_m^2)} \right), \end{aligned} \tag{B.2-8}$$

$$\begin{aligned} \frac{\partial \ln f}{\partial \sigma_m} &= \frac{\partial \ln f}{\partial \mu} \frac{\partial \mu}{\partial \sigma_m} + \frac{\partial \ln f}{\partial \sigma} \frac{\partial \sigma}{\partial \sigma_m} \\ &= \frac{\ln x - \mu}{\sigma^2} \left(-\frac{\sigma_m}{\mu_m^2 + \sigma_m^2} \right) + \left(-\frac{1}{\sigma} + \frac{(\ln x - \mu)^2}{\sigma^3} \right) \left(\frac{\sigma_m}{\sigma(\mu_m^2 + \sigma_m^2)} \right), \end{aligned} \tag{B.2-9}$$

B.3. Partial derivative of the likelihood-ratio of the copula coupled lognormal distribution and Gamma distribution to μ_m and σ_m

The concrete peak strength and peak strain are considered dependent and modelled using the 90° Clayton copula:

$$f(x, y) = c_{\theta}^{90}(u, v)f(x)f(y), \tag{B.3-1}$$

where

$$c_{\theta}^{90}(u, v) = (1 + \theta)[(1 - u)v]^{-1-\theta} [(1 - u)^{-\theta} + v^{-\theta} - 1]^{-2-1/\theta}, \tag{B.3-2}$$

where θ is the copula model parameter, with ρ_{12} being 0.9411; $u(x)$ and $v(y)$ equals to the cumulative density of the concrete peak strength $F(x)$ and peak strain $F(y)$, respectively; $f(x)$ is the lognormal PDF, defined in Eq. (B.2-1), while $f(y)$ is the Gamma PDF, defined below:

$$f(y) = \frac{y^{a-1}}{b^a \Gamma(a)} \exp\left(-\frac{y}{b}\right), \tag{B.3-3}$$

B.3.1. $\partial \ln c_{\theta}^{90}(u, v) / \partial \mu_m$ and $\partial \ln c_{\theta}^{90}(u, v) / \partial \sigma_m$ for concrete peak strength

$$\frac{\partial \ln c}{\partial u} = \frac{1 + \theta}{1 - u} - \frac{(2\theta + 1)(1 - u)^{-\theta-1}}{(1 - u)^{-\theta} + v^{-\theta} - 1} = A_1(u, v), \tag{B.3-4}$$

$$\frac{\partial u}{\partial \mu} = \phi\left(\frac{\ln x - \mu}{\sigma}\right) \frac{-1}{\sigma}, \tag{B.3-5}$$

$$\frac{\partial u}{\partial \sigma} = \phi\left(\frac{\ln x - \mu}{\sigma}\right) \frac{-(\ln x - \mu)}{\sigma^2}, \tag{B.3-6}$$

where, $\phi(\cdot)$ is the standard normal PDF function, the derivative of the standard normal cumulative density function $\Phi(\cdot)$, as $u = \Phi(x) = \Phi[(\ln x - \mu) / \sigma]$. Besides, considering Eqs. (B.2-4) to (B.2-7), the derivatives become:

$$\begin{aligned} \frac{\partial \ln c}{\partial \mu_m} &= \frac{\partial \ln c}{\partial u} \left(\frac{\partial u}{\partial \mu} \frac{\partial \mu}{\partial \mu_m} + \frac{\partial u}{\partial \sigma} \frac{\partial \sigma}{\partial \mu_m} \right) \\ &= A_1(u, v) \phi\left(\frac{\ln x - \mu}{\sigma}\right) \left[-\frac{\mu_m^2 + 2\sigma_m^2}{\sigma \mu_m (\mu_m^2 + \sigma_m^2)} + \frac{(\ln x - \mu) \sigma_m^2}{\sigma^3 \mu_m (\mu_m^2 + \sigma_m^2)} \right], \end{aligned} \tag{B.3-7}$$

$$\begin{aligned} \frac{\partial \ln c}{\partial \sigma_m} &= \frac{\partial \ln c}{\partial u} \left(\frac{\partial u}{\partial \mu} \frac{\partial \mu}{\partial \sigma_m} + \frac{\partial u}{\partial \sigma} \frac{\partial \sigma}{\partial \sigma_m} \right) \\ &= A_1(u, v) \phi\left(\frac{\ln x - \mu}{\sigma}\right) \left[\frac{\sigma_m}{\sigma (\mu_m^2 + \sigma_m^2)} - \frac{(\ln x - \mu) \sigma_m}{\sigma^3 (\mu_m^2 + \sigma_m^2)} \right]. \end{aligned} \tag{B.3-8}$$

B.3.2. $\partial \ln f(x, y) / \partial \mu_m$ and $\partial \ln f(x, y) / \partial \sigma_m$

$$\begin{aligned} \frac{\partial \ln f(x, y)}{\partial \mu_m} &= \frac{\partial \ln c}{\partial \mu_m} + \frac{\partial \ln f(x)}{\partial \mu_m} \\ &= A_1(u, v) \phi\left(\frac{\ln x - \mu}{\sigma}\right) \left[-\frac{\mu_m^2 + 2\sigma_m^2}{\sigma \mu_m (\mu_m^2 + \sigma_m^2)} + \frac{(\ln x - \mu) \sigma_m^2}{\sigma^3 \mu_m (\mu_m^2 + \sigma_m^2)} \right] \\ &+ \frac{\ln x - \mu}{\sigma^2} \frac{\mu_m^2 + 2\sigma_m^2}{\mu_m (\mu_m^2 + \sigma_m^2)} + \left(-\frac{1}{\sigma} + \frac{(\ln x - \mu)^2}{\sigma^3} \right) \left(-\frac{\sigma_m^2}{\sigma \mu_m (\mu_m^2 + \sigma_m^2)} \right), \end{aligned} \tag{B.3-9}$$

$$\begin{aligned} \frac{\partial \ln f(x, y)}{\partial \sigma_m} &= \frac{\partial \ln c}{\partial \sigma_m} + \frac{\partial \ln f(x)}{\partial \sigma_m} \\ &= A_1(u, v) \phi\left(\frac{\ln x - \mu}{\sigma}\right) \left[\frac{\sigma_m}{\sigma (\mu_m^2 + \sigma_m^2)} - \frac{(\ln x - \mu) \sigma_m}{\sigma^3 (\mu_m^2 + \sigma_m^2)} \right] \\ &+ \frac{\ln x - \mu}{\sigma^2} \left(-\frac{\sigma_m}{\mu_m^2 + \sigma_m^2} \right) + \left(-\frac{1}{\sigma} + \frac{(\ln x - \mu)^2}{\sigma^3} \right) \left(\frac{\sigma_m}{\mu_m (\mu_m^2 + \sigma_m^2)} \right), \end{aligned} \tag{B.3-10}$$

where, $\partial \ln f(x) / \partial \mu_m$ and $\partial \ln f(x) / \partial \sigma_m$ can refer to Eqs. (B.2-8) and (B.2-9), respectively.

B.3.3. $\partial \ln c_{\theta}^{90}(u, v) / \partial \mu$ and $\partial \ln c_{\theta}^{90}(u, v) / \partial \sigma$ for concrete peak strain

$$\frac{\partial \ln c}{\partial v} = -\frac{1 + \theta}{v} + \frac{(2\theta + 1)v^{-\theta-1}}{(1 - u)^{-\theta} + v^{-\theta} - 1}, \tag{B.3-11}$$

$$\frac{\partial v}{\partial a} = \frac{1}{\Gamma(a)} \int_0^y t^{a-1} e^{-t} \ln t dt - \psi(a)v, \tag{B.3-12}$$

$$\frac{\partial v}{\partial b} = -\frac{y}{b} f(y), \tag{B.3-13}$$

$$\frac{\partial a}{\partial \mu} = 2 \frac{\mu}{\sigma^2}, \tag{B.3-14}$$

$$\frac{\partial b}{\partial \mu} = -\frac{\sigma^2}{\mu^2}, \tag{B.3-15}$$

$$\frac{\partial a}{\partial \sigma} = -2 \frac{\mu^2}{\sigma^3}, \tag{B.3-16}$$

$$\frac{\partial b}{\partial \sigma} = 2 \frac{\sigma}{\mu}. \tag{B.3-17}$$

Then, the copula term's derivatives are:

$$\begin{aligned} \frac{\partial \ln c}{\partial \mu} &= \frac{\partial \ln c}{\partial v} \left(\frac{\partial v}{\partial a} \frac{\partial a}{\partial \mu} + \frac{\partial v}{\partial b} \frac{\partial b}{\partial \mu} \right) \\ &= \left(-\frac{1+\theta}{v} + \frac{(2\theta+1)v^{-\theta-1}}{(1-u)^{-\theta} + v^{-\theta} - 1} \right) \left[2 \frac{\mu}{\sigma^2} \left(\frac{1}{\Gamma(a)} \int_0^y t^{a-1} e^{-t} \ln t dt - \psi(a)v \right) + \frac{\sigma^2}{\mu^2} \frac{y}{b} f(y) \right], \end{aligned} \tag{B.3-18}$$

$$\begin{aligned} \frac{\partial \ln c}{\partial \sigma} &= \frac{\partial \ln c}{\partial v} \left(\frac{\partial v}{\partial a} \frac{\partial a}{\partial \sigma} + \frac{\partial v}{\partial b} \frac{\partial b}{\partial \sigma} \right) \\ &= \left(-\frac{1+\theta}{v} + \frac{(2\theta+1)v^{-\theta-1}}{(1-u)^{-\theta} + v^{-\theta} - 1} \right) \left[-2 \frac{\mu^2}{\sigma^3} \left(\frac{1}{\Gamma(a)} \int_0^y t^{a-1} e^{-t} \ln t dt - \psi(a)v \right) - 2 \frac{\sigma}{\mu} \frac{y}{b} f(y) \right]. \end{aligned} \tag{B.3-19}$$

B.3.4. Partial derivative of the likelihood ratio of the gamma distribution to μ and σ

Given the distribution function in Eq. (B.3-3), the derivatives are:

$$\frac{\partial \ln f}{\partial a} = \ln y - \ln b - \psi(a), \tag{B.3-20}$$

$$\frac{\partial \ln f}{\partial b} = \frac{y-ab}{b^2}. \tag{B.3-21}$$

Also considering Eqs. (B.3-14) to (B.3-17), the likelihood ratio of distribution derivatives to μ and σ are:

$$\begin{aligned} \frac{\partial \ln f}{\partial \mu} &= \frac{\partial \ln f}{\partial a} \frac{\partial a}{\partial \mu} + \frac{\partial \ln f}{\partial b} \frac{\partial b}{\partial \mu} \\ &= 2 \frac{\mu}{\sigma^2} (\ln y - \ln b - \psi(a)) - \frac{\sigma^2}{\mu^2} \frac{y-ab}{b^2}, \end{aligned} \tag{B.3-22}$$

$$\begin{aligned} \frac{\partial \ln f}{\partial \sigma} &= \frac{\partial \ln f}{\partial a} \frac{\partial a}{\partial \sigma} + \frac{\partial \ln f}{\partial b} \frac{\partial b}{\partial \sigma} \\ &= -2 \frac{\mu^2}{\sigma^3} (\ln y - \ln b - \psi(a)) + 2 \frac{\sigma}{\mu} \frac{y-ab}{b^2}. \end{aligned} \tag{B.3-23}$$

B.3.5. $\partial \ln f(x, y) / \partial \mu$ and $\partial \ln f(x, y) / \partial \sigma$

$$\begin{aligned} \frac{\partial \ln f(x, y)}{\partial \mu} &= \frac{\partial \ln c}{\partial \mu} + \frac{\partial \ln f(y)}{\partial \mu} \\ &= \left(-\frac{1+\theta}{v} + \frac{(2\theta+1)v^{-\theta-1}}{(1-u)^{-\theta} + v^{-\theta} - 1} \right) \left[2 \frac{\mu}{\sigma^2} \left(\frac{1}{\Gamma(a)} \int_0^y t^{a-1} e^{-t} \ln t dt - \psi(a)v \right) + \frac{\sigma^2}{\mu^2} \frac{y}{b} f(y) \right] \\ &\quad + 2 \frac{\mu}{\sigma^2} (\ln y - \ln b - \psi(a)) - \frac{\sigma^2}{\mu^2} \frac{y-ab}{b^2}, \end{aligned} \tag{B.3-24}$$

$$\begin{aligned} \frac{\partial \ln f(x, y)}{\partial \sigma} &= \frac{\partial \ln c}{\partial \sigma} + \frac{\partial \ln f(y)}{\partial \sigma} \\ &= \left(-\frac{1+\theta}{v} + \frac{(2\theta+1)v^{-\theta-1}}{(1-u)^{-\theta} + v^{-\theta} - 1} \right) \left[-2 \frac{\mu^2}{\sigma^3} \left(\frac{1}{\Gamma(a)} \int_0^y t^{a-1} e^{-t} \ln t dt - \psi(a)v \right) - 2 \frac{\sigma}{\mu} \frac{y}{b} f(y) \right] \\ &\quad - 2 \frac{\mu^2}{\sigma^3} (\ln y - \ln b - \psi(a)) + 2 \frac{\sigma}{\mu} \frac{y-ab}{b^2}. \end{aligned} \tag{B.3-25}$$

B.4. Partial derivative of the likelihood ratio of the normal distribution to μ and σ

$$f(x) = \frac{1}{\sigma\sqrt{2\pi}} \exp\left[-\frac{(x-\mu)^2}{2\sigma^2}\right], \quad (\text{B.4-1})$$

$$\frac{\partial \ln f}{\partial \mu} = \frac{x-\mu}{\sigma^2}, \quad (\text{B.4-2})$$

$$\frac{\partial \ln f}{\partial \sigma} = -\frac{1}{\sigma} + \frac{(x-\mu)^2}{\sigma^3}. \quad (\text{B.4-3})$$

Data availability

No data was used for the research described in the article.

References

- [1] Pearson C, Delatte N. Ronan point apartment tower collapse and its effect on building codes. *J Perform Constr Facil* 2005;19(2):172–7.
- [2] Omika Y, Fukuzawa E, Koshika N, Morikawa H, Fukuda R. Structural responses of world trade center under aircraft attacks. *J Struct Eng* 2005;131(1):6–15.
- [3] Lu XZ, Guan H, Sun HL, Li Y, Zheng Z, Fei YF, et al. A preliminary analysis and discussion of the condominium building collapse in surfside, Florida, US, June 24, 2021. *Front Struct Civ Eng* 2021;15:1097–110.
- [4] HM Government. The building regulations 2010: Approved document A. London, UK: HM Government; 2013. Section A3: Disproportionate collapse.
- [5] State Administration for Market Regulation (SAMR) Standardization Administration of the People's Republic of China (SAC). GB/T 228.1-2021 Metallic materials—Tensile testing—Part. 1: Method of test at room temperature. Beijing, China; 2021.
- [6] Department of Defense (DoD). Unified facilities criteria (UFC) 4-023-03: Design of buildings to resist progressive collapse. Washington, DC: U.S. Department of Defense; 25 Jan 2005.
- [7] European Committee for Standardization (CEN). EN 1991-1-7 Eurocode 1: Actions on structures, Part 1-7: General actions - accidental actions, Brussels, Belgium: CEN; 2006.
- [8] United States General Services Administration (GSA). Progressive collapse analysis and design guidelines for new federal office buildings and major modernization projects. Washington, DC: U.S. General Services Administration; Jun 2003.
- [9] Su YP, Tian Y, Song XS. Progressive collapse resistance of axially-restrained frame beams. *ACI Struct J* 2009;106(5):600–7.
- [10] Kang SB, Tan KH. Analytical study on reinforced concrete frames subject to compressive arch action. *Eng Struct* 2017;141:373–85.
- [11] Lu XZ, Lin KQ, Li CF, Li Y. New analytical calculation models for compressive arch action in reinforced concrete structures. *Eng Struct* 2018;168:721–35.
- [12] Yi WJ, He QF, Xiao Y, Kunnath SK. Experimental study on progressive collapse-resistant behavior of reinforced concrete frame structures. *ACI Struct J* 2008;105:433–9.
- [13] Li Y, Lu XZ, Guan H, Ye LP. Progressive collapse resistance demand of RC frames under catenary mechanism. *ACI Struct J* 2014;111(5):1225–34.
- [14] Long X, Wang S, Huang X-J, Li C, Kang S-B. Progressive collapse resistance of exterior reinforced concrete frames and simplified method for catenary action. *Eng Struct* 2021;249:113316.
- [15] Gan YP, Chen J, Xiang MJ. PDEM-based reliability assessment of RC frames against progressive collapse considering initial local failure. *J Build Eng* 2023;76:107198.
- [16] Zhou Y, Zhang BZ, Luo XM, Hwang H-J, Zheng P, Zhu ZR, et al. Reliability of fully assembled precast concrete frame structures against progressive collapse. *J Build Eng* 2022;51:104362.
- [17] Brunesi E, Nascimbene R, Parisi F, Augenti N. Progressive collapse fragility of reinforced concrete framed structures through incremental dynamic analysis. *Eng Struct* 2015;104:65–79.
- [18] Li Y, Lu XZ, Guan H, Ren PQ, Qian LP. Probability-based progressive collapse-resistant assessment for reinforced concrete frame structures. *Adv Struct Eng* 2016;19:1723–35.
- [19] Yu XH, Lu DG, Qian K, Li B. Uncertainty and sensitivity analysis of reinforced concrete frame structures subjected to column loss. *J Perform Constr Facil* 2017;31:04016069.
- [20] Feng DC, Xie SC, Xu J, Qian K. Robustness quantification of reinforced concrete structures subjected to progressive collapse via the probability density evolution method. *Eng Struct* 2020;202:109877.
- [21] Lin KQ, Chen ZF, Li Y, Lu XZ. Uncertainty analysis on progressive collapse of RC frame structures under dynamic column removal scenarios. *J Build Eng* 2022;46:103811.
- [22] Ding LC, Van Coile R, Botte W, Caspele R. Quantification of model uncertainties of the energy-based method for dynamic column removal scenarios. *Eng Struct* 2021;237:112057.
- [23] Ding LC, Chen JB. Physically-based collapse failure criteria in progressive collapse analyses of random-parameter multi-story RC structures subjected to column removal scenarios. *Eng Struct* 2025;325:119379.
- [24] Ribeiro LDR, Kroetz HM, Parisi F, Beck AT. Optimal risk-based design of reinforced concrete beams against progressive collapse. *Eng Struct* 2024;300:117158.
- [25] Zhou Y, Chen TP, Pei YL, Hwang H-J, Hu X, Yi WJ, et al. Static load test on progressive collapse resistance of fully assembled precast concrete frame structure. *Eng Struct* 2019;200:109719.
- [26] Lew HS, Main JA, Bao Y, hai, Sadek F, Chiarito VP, Robert SD, Torres JO. Performance of precast concrete moment frames subjected to column removal: part 1, experimental study. *PCI J* 2017;62:35–52.
- [27] Qian K, Liang SL, Fu F, Fang Q. Progressive collapse resistance of precast concrete beam-column sub-assemblages with high-performance dry connections. *Eng Struct* 2019;198:109552.
- [28] Bao Y, Tan KH. Performance of precast concrete beam-column joint with a hidden corbel under progressive collapse scenarios. *Eng Struct* 2022;267:114679.
- [29] Zhao ZD, Cheng XW, Li Y, Diao MZ, Guan H, Zhang WJ, et al. Progressive collapse resistance of precast concrete beam-column assemblies using dry connections under uniformly distributed loading condition. *Eng Struct* 2024;306:117820.
- [30] Liu YL, Zhao ZD, Cheng XW, Li Y, Diao MZ, Sun HL. Experimental and numerical investigation of the progressive collapse of precast reinforced concrete frame substructures with wet connections. *Eng Struct* 2022;256:114010.
- [31] Zhao ZD, Cheng XW, Li Y, Diao M, Guan H, An Y. Progressive collapse analysis of precast reinforced concrete beam-column assemblies with different dry connections. *Eng Struct* 2023;287:116174.
- [32] Nimse RB, Joshi DD, Patel PV. Experimental study on precast beam column connections constructed using RC corbel and steel billet under progressive collapse scenario. *Struct Congr, Portland, Oregon: American Society of Civil Engineers; 2015. p. 1101–17.*
- [33] Almusallam TH, Elsanadedy HM, Al-Salloum YA, Siddiqui NA, Iqbal RA. Experimental investigation on vulnerability of precast RC beam-column joints to progressive collapse. *KSCE J Civ Eng* 2018;22:3995–4010.
- [34] Bao YH, Main JA, Lew HS, Sadek F. Performance of precast concrete moment frames subjected to column removal: part 2, computational analysis. *PCI J* 2017;62:53–74.
- [35] Qian K, Li B. Investigation into resilience of precast concrete floors against progressive collapse. *ACI Struct J* 2019;116:171–82.
- [36] Dang C, Wei PF, Song JW, Beer M. Estimation of failure probability function under imprecise probabilities by active learning-augmented probabilistic integration. *ASCE-ASME J Risk Uncertain Eng Syst Part Civ Eng* 2021;7:04021054.
- [37] Dang C, Wei PF, Faes MGR, Valdebenito MA, Beer M. Parallel adaptive Bayesian quadrature for rare event estimation. *Reliab Eng Syst Saf* 2022;225:108621.
- [38] Zhao ZD, Cheng XW, Li Y, Diao M, Liu YL, Zhang WJ. Robustness analysis of dynamic progressive collapse of precast concrete beam-column assemblies using dry connections under uniformly distributed load. *Eng Struct* 2025;323:119206.
- [39] Yu J, Luo LZ, Li Y. Numerical study of progressive collapse resistance of RC beam-slab substructures under perimeter column removal scenarios. *Eng Struct* 2018;159:14–27.
- [40] Pham AT, Tan KH, Yu J. Numerical investigations on static and dynamic responses of reinforced concrete sub-assemblages under progressive collapse. *Eng Struct* 2017;149:2–20.
- [41] Pham AT, Tan KH. Static and dynamic responses of reinforced concrete structures under sudden column removal scenario subjected to distributed loading. *J Struct Eng* 2019;145:04018235.
- [42] Qian K, Geng SY, Liang SL, Fu F, Yu J. Effects of loading regimes on the structural behavior of RC beam-column sub-assemblages against disproportionate collapse. *Eng Struct* 2022;251:113470.
- [43] Bao YH, Main JA, Lew HS, Sadek F. Modeling of reinforced concrete assemblies under column-removal scenario. *J Struct Eng* 2017;62(5):53–74.
- [44] Mander JB, Priestley MJN, Park R. Theoretical stress-strain model for confined concrete. *J Struct Eng* 1988;114:1804–26.
- [45] Ministry of Housing and Urban-Rural Development of the People's Republic of China (MOHURD). GB 50068-2018 Unified standard for reliability design of building structures. Beijing, China; 2018.
- [46] Zhong CT, Li G, Meng Z, Li HJ, Yildiz AR, Mirjalili S. Starfish optimization algorithm (SFO): a bio-inspired metaheuristic algorithm for global optimization compared with 100 optimizers. *Neural Comput & Applic* 2025;37:3641–83.

- [47] Tao JJ, Chen JB, Ren XD. Copula-based quantification of probabilistic dependence configurations of material parameters in damage constitutive modeling of concrete. *J Struct Eng* 2020;146:04020194.
- [48] Lyu MZ, Chen JB, Shen JX. Refined probabilistic response and seismic reliability evaluation of high-rise reinforced concrete structures via physically driven dimension-reduced probability density evolution equation. *Acta Mech* 2024;235:1535–61.
- [49] Mirza SA, MacGregor JG. Variability of mechanical properties of reinforcing bars. *J Struct Div* 1979;105:921–37.
- [50] Marelli S, Sudret B. UQLab: a framework for uncertainty quantification in Matlab. *Vulnerability Uncertain. Risk*, Liverpool, UK: American Society of Civil Engineers; 2014. p. 2554–63.
- [51] Rubinstein RY. Sensitivity Analysis and Performance Extrapolation for Computer simulation Models. *Oper Res* 1989;37:72–81.
- [52] Li JH, Mosleh A, Kang R. Likelihood ratio gradient estimation for dynamic reliability applications. *Reliab Eng Syst Saf* 2011;96:1667–79.
- [53] Rubinstein RY, Kroese DP. *Simulation and the Monte Carlo method*. 3rd edition. Hoboken NJ: John Wiley & Sons; 2017.